# Effects of Particle Shape on the Shear Behaviour and Breakage of Ballast: DEM Approach

**Jing Chen**, PhD
Postdoc research fellow, Department of Civil Engineering, Zhejiang University, Hangzhou, China; Former visiting PhD student, Centre for Geomechanics and Railway Engineering, Faculty of Engineering and Information Science, University of Wollongong, Wollongong City, Australia. Email: j.chen9412@zju.edu.cn

**Buddhima Indraratna**, PhD (Alberta), FTSE, FIEAust, FASCE, FGS
Distinguished Professor of Civil Engineering and Director of Transport Research Centre, University of Technology Sydney, Ultimo, Australia; Founding Director, ARC Industrial Transformation Training Centre for Advanced Technologies in Rail Track Infrastructure (ITTC-Rail). Email: Buddhima.Indraratna@uts.edu.au

**Jayan S. Vinod**, PhD, MASCE, MAGS, MIGS, ISSMGE
Associate Professor, Centre for Geomechanics and Railway Engineering, Faculty of Engineering and Information Sciences, University of Wollongong, Wollongong City, Australia. Email: vinod@uow.edu.au

**Trung Ngo**, PhD, MASCE
Senior lecturer, Transport Research Centre, School of Civil and Environmental Engineering, University of Technology Sydney, Ultimo, Australia. Email: Trung.Ngo@uts.edu.au

**Yangzepeng Liu**, PhD
Postdoc research fellow, China Railway 11th Bureau Group Co Ltd, Wuchang District, Wuhan, China.
Email: lyzpcwl@hotmail.com

**Technical Paper,** Submitted to ASCE-International Journal of Geomechanics

Author for correspondence:

Distinguished Professor Buddhima Indraratna

Transport Research Centre

University of Technology Sydney

Ultimo, NSW 2007

Australia.

Ph: +61 2 9514 8000

Email: buddhima.indraratna@uts.edu.au

# Effects of particle shape on the shear behaviour and breakage of ballast: DEM approach

Jing Chen[a,c], Buddhima Indraratna[b,*], Jayan S. Vinod[c], Trung Ngo[b], Yangzepeng Liu[d]

[a]*Department of Civil Engineering, Zhejiang University, Hangzhou 310058, China*

[b]*Transport Research Centre, Faculty of Engineering and Information Technology, University of Technology Sydney, Sydney, NSW 2007, Australia*

[c]*Centre for Geomechanics and Railway Engineering, Faculty of Engineering and Information Sciences, University of Wollongong, Wollongong City, NSW 2522, Australia*

[d]*China Railway 11th Bureau Group Co Ltd, Wuchang District, Wuhan 430072, China*

ABSTRACT:

This paper presents results obtained from Discrete Element Method (DEM) to study the effects of particle shape on the shear behaviour and breakage of ballast aggregates. In this study, a series of direct shear testing is performed on granular assemblies having various shape sphericities and roundness. A clump-based degradation (breakage) model is incorporated into the DEM simulation to capture the breakage of aggregates during shearing. The results show that the decrease of particle sphericity and roundness (angularity) results in an improvement in the shear performance of granular assemblies but subsequent exacerbation in particle breakage, which in turn reduces the shear strength and volumetric dilation. The breakage of particles localizes within an inclined band, with the width and the inclination angle of the band increasing in assemblies comprising particles of low sphericity and roundness. A micromechanical analysis is conducted to examine the anisotropy of internal structures and particle motions in granular assemblies. It is observed that both the shape of particles and their breakage significantly influence these factors. Through the microscopic analysis, a fundamental governing mechanism of particle shape effects on the shear strength and the breakage of granular materials is investigated at macroscopic scale.

*Keywords*: Particle breakage; Sphericity and roundness; Shear behaviour; Anisotropy of internal structure; Discrete element method

---

*Corresponding author
*Email address*: Buddhima.Indraratna@uts.edu.au (Buddhima Indraratna)

## 1. Introduction

The importance of particle shape in influencing the shear behaviour of granular materials has been extensively studied by many existing studies. For example, in geotechnical engineering, the shape of particles can affect the shear strength, permeability, abrasion resistance of sands, rockfills and railway ballast materials (Bono and McDowell 2016; Chen et al. 2019; Rui et al. 2020; Taiba et al. 2018; Yang and Luo 2015). In the pharmaceutical, food, and chemical industries, particle shape is considered to be a key factor to influence the flowability, mixing, and processing of powders (Ketterhagen et al. 2009). The shape of particles can also affect the packing density and diffusion behaviour of granular materials used in energy storage applications such as lithiumion batteries and supercapacitors (Zhang et al. 2022). Moreover, the shape of particles has also reported to affect the filtration efficiency an flow resistance of granular media used in water treatment and wastewater treatment processes (Hamidian et al. 2021).

In geotechnical engineering field, the shear behaviour of geomaterials often governs the strength and deformation characteristics of the assemblies. (Cho et al. 2006) and (Altuhafi et al. 2016) compiled several databases containing natural sands of different shapes to comprehensively study particle shape effects on the shear behaviour of sand materials. A series of shape-dependent parameter correlations have been provided in their studies to justify particle shape effects on grain packing and mechanical parameters including the extreme void ratios $e_{\max}$ and $e_{\min}$, the shear wave velocity $V_s$, the compression and decompression indices $C_c$ and $C_s$, and three parameters of critical state line $\Gamma$, $\lambda$, and $\phi_{cs}$. A series of direct shear box testing was performed by (Li 2013) on sands mixed with clays and crushed granite gravels, by which the effect of particle shape on the shear strength of composite soils was explored. Besides the packing and strength characteristics of granular materials, the shape of particles also affects their interface shear behaviour with other geosynthetics (Liu et al. 2021a; Miao et al. 2017; Namjoo et al. 2022) or structures (Liu et al. 2022).

Numerical simulation methods such as the Discrete Element Method (DEM) has been widely applied to study the mechanical behaviour of granular materials at microscopic scales, where the angularity and breakage of particles can be simulated. There have been numerous studies conducted to investigate the effects of particle shape on the shear behaviour of granular materials (Coetzee 2016; Danesh et al. 2020; Gong et al. 2019; Liu et al. 2019; Wu et al. 2021). They reported that the increase in particle angularity leads to an improved shearing performance of granular materials because of the enhanced inter-particle interlocking. The shape of particles also plays a crucial role in influencing the microscopic responses of granular materials during shearing (Nuebel and Rothenburg 1996). (Zhao et al. 2017) performed a series of shearing tests on granular pakcings comprising super-ellipsoids with various shapes, and investigated the shape effects on the internal structure characteristics of granular materials. (Xu et al. 2021) investigated the influence of particle shape on the fabric anisotropy of granular materials at their critical states, and found that the critical fabric anisotropy of assemblies decreases with the increase of particle aspect ratio. A study conducted by (Yang et al. 2016) showed that particle shape directly influences the strain localization patterns, fabric distributions, and probability distribution of the normalized contact forces within granular assemblies.

Particle degradation (breakage) is another salient feature of granular materials and plays a significant role in influencing the mechanical behaviour of granular assemblies (Chen et al. 2022; Coop et al. 2004; Indraratna et al. 2009; Mcdowell 2002). However, the influence of particle shape effect on particle degradation has not been considered in the above-mentioned studies. (Sun and Zheng 2017) analyzed the breakage-induced shape evolution of ballast aggregates subjected to triaxial compression by using fractal theory. (Jo et al. 2011) found that the shape of particles affects the formation of shear band within crushable assemblies. (Jing et al. 2020) simulated ballast aggregates with different flakiness and elongation indices in DEM, and found that flaky and elongated aggregates produce more particle breakage among all the tested ballast materials. (Nie et al. 2020) simulated the shear behaviour of granular materials with different shapes caused by natural erosion process, and found that an increased erosion degree of particles results in the decrease in the shear strength and volumetric deformation. There are some studies showing that the shape of particles influences not only their breakage strength but also their breakage patterns (Afshar et al. 2017; Zhang et al. 2020). A recent study carried out by (Seyyedan et al. 2023) using the coupled DEM and extended Finite Element Method (XFEM) showed that the angularity and the eccentricity of particles significantly affect the particle breakage and mechanical behaviour of rock-fills subjected to direct shearing.

Despite the significant progress achieved thus far, the influence of particle shape on the shear behaviour of granular materials, particularly their breakage responses and the microscopic characteristics of aggregates, remains unclear. To address this gap, this study employs a series of direct shearing tests on aggregates with varying shapes and sizes using the DEM. The investigation encompasses an examination of strength, deformation, and breakage band characteristics for granular materials with different sphericities and roundnesses. Additionally, the microscopic properties of aggregates, including internal structure anisotropy and particle motion are analysed, through which the mutual influence mechanism of particle shape effects on the macroscopic mechanical behaviour of granular materials is investigated from a particulate perspective.

## 2. Discrete element modeling

### *2.1 Modelling irregularly-shaped particles in DEM*

To capture a high irregularity and angularity of quarried ballast having different shapes and sizes, an X-Ray computed tomography (CT) scanning machine with a resolution of 0.3 mm × 0.3 mm × 0.6 mm per voxel was adopted. After scanning, an image-based processing strategy as detailed by (Chen et al. 2019) was applied to reconstruct the irregular morphology of ballast particles. Fig. 1(a and b) shows the images of five typical ballast particles and their representative slices taken across the bodies. The obtained greyscale images were then binarized by converting the particle solid into white and the background into black, and an algorithm based on the 8-adjacency area method (Ege and Karaca 2016) was developed to automatically extract the particle solid contours, as shown in Fig. 1(c). To represent the irregular shapes of ballast particles in DEM, a group of spheres of varying sizes were clumped together within the contour using the 'Bubble Pack' algorithm (Taghavi 2011). Two parameters, the minimum radius ratio $\rho = 0.1$, which represents the size ratio of the smallest to largest pebble in the clump, and the maximum intersection angle $\varphi = 135°$, which describes the distance between two intersecting pebbles, were used to govern the precision of the generated particles. The images of five typical particle clumps are shown in Fig. 1(c), and a total of 40 ballast particles of various shapes were prepared for this study.

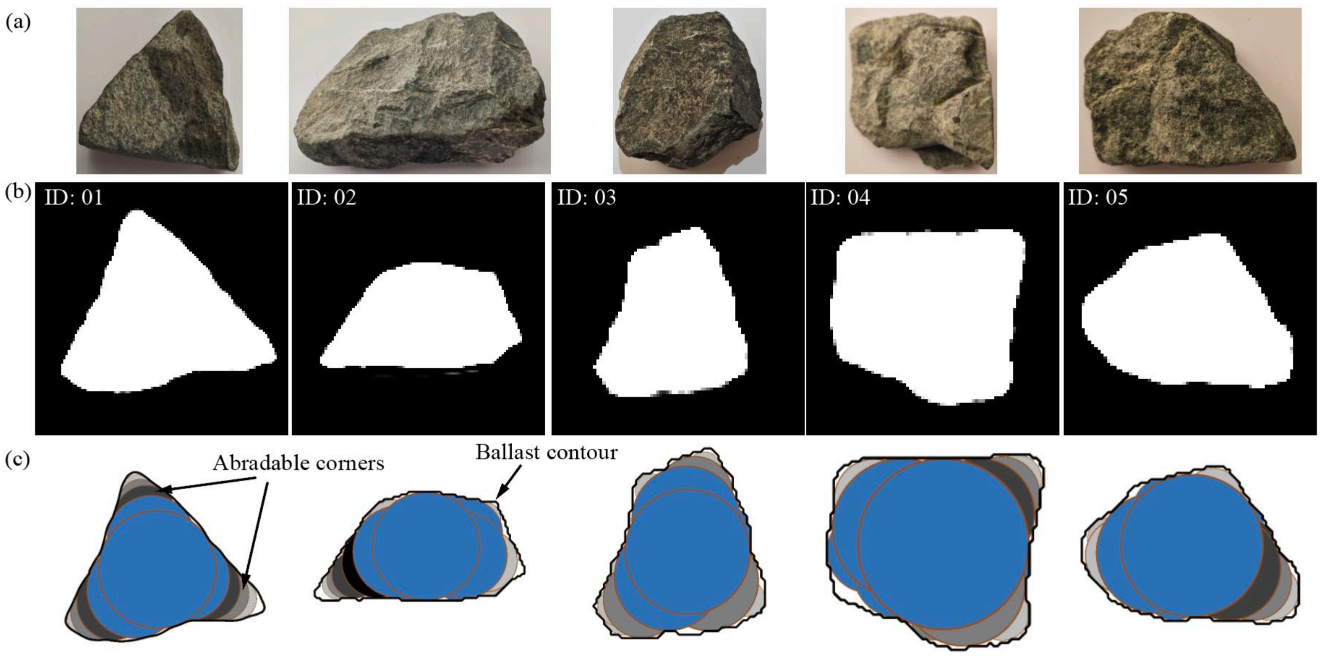


**Fig. 1.** (a) Images of five typical ballast particles; (b) CT scanning slices; and (c) created clumps used

in DEM simulations

*2.2 Particle shape quantification*

Particle shape can be fully quantified by three independent sub-quantities, with each describing the shape at different scales or orders. The large scale (first order) focuses on the overall form/ morphology of the particle, and the commonly adopted quantities for large scale include sphericity (Wadell 1933), elongation (Zingg 1935), etc. An intermediate-scale (second order) quantity, such as roundness or angularity (Powers 1953), describes the properties of sharp corners and edges on the particle boundaries. The smallest scale (third order) focuses on the surface texture or the particle roughness (Alshibli and Alsaleh 2004). Among the three-scale parameters, particle sphericity and roundness have been acknowledged as the most important quantities as they directly govern the macro and microscopic mechanical behaviour of granular materials (Guo et al. 2022). Therefore, the sphericity and roundness values of ballast particles will be considered in the current DEM analysis.

There are various sphericity parameters that have been proposed in the past, and they can be broadly classified into two categories based on principal dimensions (such as Feret's diameter, Aspect Ratio, or Circle Ratio) or overall geometry properties (such as surface area, perimeter or volume). To increase the credibility of description on particle sphericity, two sphericity parameters as suggested by (Liu et al. 2019), the circle ratio ($S_c$) and the area sphericity ($S_a$), has been adopted. The $S_c$ and $S_a$ of the 40 selected ballast particles were calculated as given by:

$$S_c = \frac{D_{ins}}{D_{cir}} \quad (1)$$

$$S_a = \frac{A_s}{A_{cir}} \quad (2)$$

Where, $D_{ins}$ and $D_{cir}$ are the diameters of the largest inscribed circle and the smallest circumscribed circle, respectively; $A_s$ and $A_{cir}$ are the areas of a particle and its smallest circumscribed circle, respectively, as shown in Fig. 2(a).

The roundness and angularity are used to describe the corners and sharp edges of a particle, with a large roundness value indicating a low level of angularity. By using the projections of particles on the 2-dimensional plane, (Wadell 1933) proposed a classic methodology to determine the roundness of a particle, as expressed by:

$$R_w = \frac{1}{N}\frac{\sum r_i}{R} \tag{3}$$

where, $N$ is the number of particle corners; $r_i$ is the radius of curvature of the corner; $R$ is the radius of the maximum inscribed circle in the plane of measurement. In this study, a technique called 'locally weighted scatter plot smoothing' (LOESS) (Zheng and Hryciw 2015) was adopted for ballast roundness computation, and the corners of ballast particles are determined, as shown in Fig. 2(a).

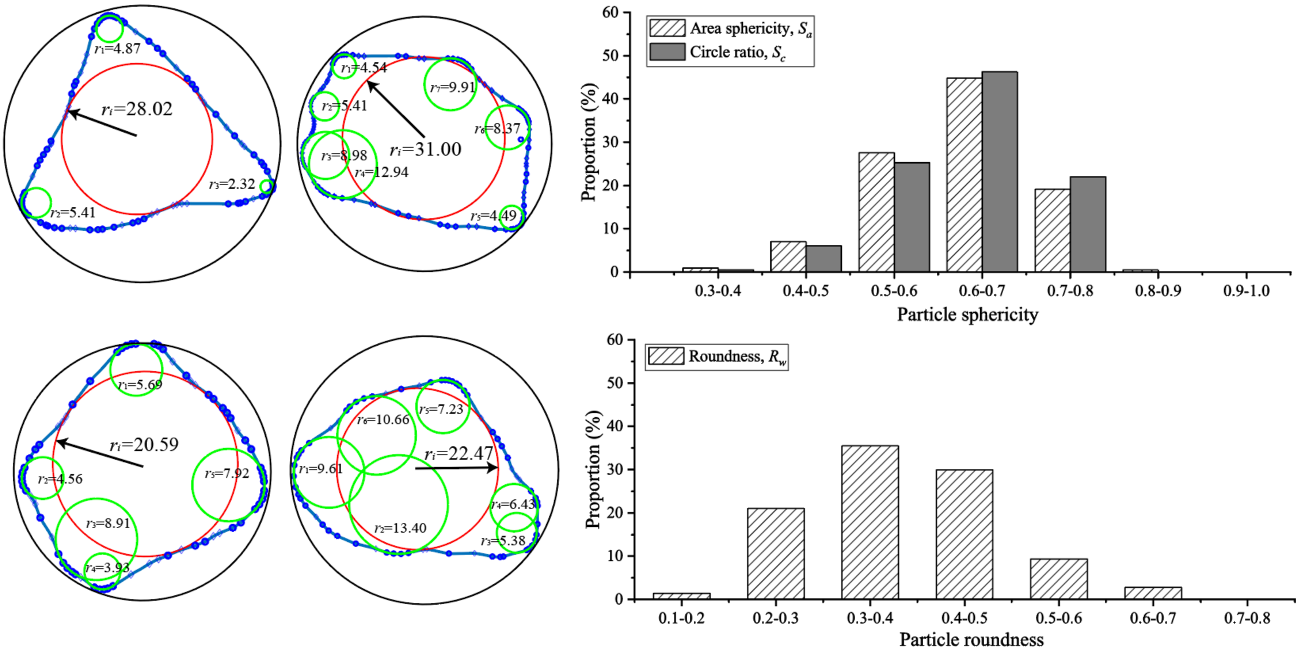


(a) (b)

**Fig. 2.** (a) Diagrams of shape quantification for 4 typical particles; and (b) distribution histograms of sphericity and roundness for 40 ballast particles

Fig. 2(b) shows the distribution histograms for the two sphericity parameters and the roundness of the 40 ballast particles. It can be seen that more than 90% of the examined ballast particles have $S_c$ and

$S_a$ values between 0.50 and 0.80, with sphericity values of 0.60~0.70 accounting for the greatest proportion. Particle roundness ranges from 0.15 to 0.50, with the majority of particles having $R_w$ of 0.30. Based on the calculated sphericity and roundness values, 40 ballast particles are classified into four groups: (i) low-sphericity-low-roundness, $S_1 - R_1$ ($0.40 \leq S_c, S_a < 0.63$ and $0.10 \leq R_w < 0.30$), (ii) low-sphericity-high-roundness, $S_1 - R_2$ ($0.40 \leq S_c, S_a < 0.63$ and $R_w \geq 0.30$), (iii) high-sphericity-low-roundness $S_2 - R_1$ ($0.63 \leq S_c, S_a < 1.0$ and $0.10 \leq R_w < 0.30$), and (iv) high-sphericity-high-roundness, $S_2 - R_2$ ($0.63 \leq S_c, S_a < 1.0$ and $R_w \geq 0.30$).

*2.3 Modelling ballast breakage in DEM*

Upon repeated train loading, ballast undergoes progressive degradation and breakage. The dominant breakage patterns of granular materials has been reported as corner abrasion or surface attrition (Sun et al. 2014). To model the breakage of rigid ballast clumps in DEM, (Liu et al. 2021b) developed a 2D abrasion model and the model has been well validated by a series of DEM simulations for Los Angeles Abrasion (LAA) testing on ballast aggregates. The proposed particle degradation model has been widely used in the existing discrete element modeling of ballast aggregates because of its superiority in capturing the corner abrasion behaviour of irregular ballast particles in the long-term and improved efficiency in computational resources (Chen et al. 2022, 2023).

According to (Liu et al. 2021b), the irregularly-shaped particles are abraded in either shearing or crushing mode based on the contact force acting on the sharp corner. The broken corner pebble will be automatically removed from the system and replaced by either one or two newly-introduced fragment balls located tangent to its parent clump if a maximum contact force criterion is satisfied. The sizes of the fragment balls are determined based on the non-overlapping volume between the broken pebble and its parent clump. A linear size expansion will be applied to the fragment balls after their introduction for the mass conservation of the entire system. The breaking sequence of pebbles in each ballast clump is represented by the color depth as shown in Fig. 1(c). In addition, to prevent ballast clump from limitless breaking, pebbles that are able to be abraded is selected and predefined based on their sizes relative to the largest pebbles in each ballast clump. Fig. 1(c) shows the potential breakable pebbles for the five typical ballast clumps, with the unbreakable parent clumps being colored as blue. The developed abrasion model was incorporated into the current DEM analysis, and it was automatically triggered during the simulation to capture the breakage of ballast aggregates during loading. The validation of the particle degradation model can refer to Section 3.

### *2.4 Direct shear test simulation*

In this study, a series of direct shear test simulations were conducted on ballast aggregates of various shapes. To allow for a clearer representation of the shear behaviour and provide valuable insights into the granular material's response under shearing conditions, the current DEM analysis was conducted using 2D modeling instead of 3D. A total of four samples were prepared by choosing ballast particles randomly from different particle groups. The samples were created by first placing overlapped circular disks with a specific certain particle size distribution (PSD) inside a rectangular shearing box having dimensions of 500 mm in height, 600 mm in width at the bottom, and 700 mm at the top, as illustrated in Fig. 3. The bottom shearing box was 100mm wider than the upper box to ensure a constant shearing area. The PSD complied with the Chinese Railway Ballast Standard (TB/T 2140-2008), which is comparable to other widely-used standards across the world, such as the Australian Standard AS 2758.7 ($d_{50} = 35$ mm). The disk clouds were initially cycled to reach their equilibrium state when the unbalanced force ratio of the entire system was less than $10^{-5}$, and the disks were then replaced by clumps of irregularly shaped ballast that had volumes equal to the corresponding disks (measured in unit thicknesses out of plane). Prior to any subsequent shearing, all the samples were preloaded under a normal pressure of 100 kPa to increase the density of the ballast aggregates.

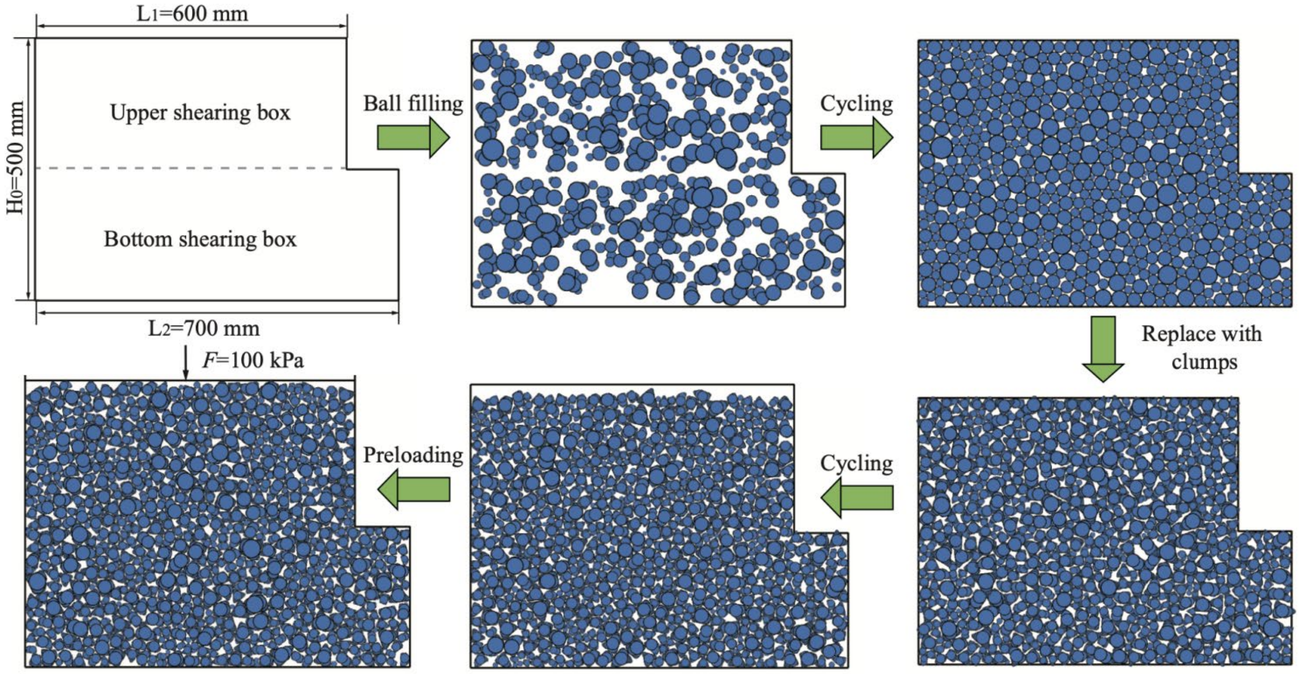


**Fig. 3.** Preparation of DEM model for direct shear test simulation

## 3. Parameter calibration and model validation

In addition to particle size and shape, the contact model and micro-mechanical parameters can also affect the accuracy of DEM simulation. In this study, a linear contact law was applied to simulate the contacts among particles. Before applying the created irregular ballast particles and the proposed degradation model to the current DEM analysis, a series of preliminary simulations on the triaxial testing (Fig. 4(a)) and the Los Angeles Abrasion (LAA) testing (Fig. 4(b)) were performed to determine the appropriate parameters for ballast aggregates and to validate the effectiveness of the particle degradation model in capturing ballast breakage behaviour.

The predicted shear stress-strain responses were compared with those obtained using large-scale triaxial testing by (Indraratna et al. 2013). A DEM model with an initial dimension of 300 mm (D) × 600 mm (H) identical to the triaxial chamber size was prepared. The ballast particles were randomly selected from the established particle library (Chen et al. 2019) for the generation of the aggregates, with its particle size distribution (PSD) following the Australian Standard for ballast, AS 2758.7 (2015). The monotonic shearing was conducted on the ballast aggregate under various values of friction coefficient ($\mu$) and normal and shear stiffness of particle contacts ($k_n$ and $k_s$), which are considered as the predominant parameters governing the stress-strain behaviour of granular materials in discrete element modeling. Fig. 4(a) shows the shear stress-strain responses predicted by the DEM model capturing particle breakage in contrast to the experimental data provided by (Indraratna et al. 2013). In essence, the DEM model simulating particle degradation has made a satisfactory prediction of the shear stress-strain response of the ballast aggregates for a given confining pressure albeit some fluctuations. The calibrated micro-mechanical parameters for ballast aggregates are summarized in Table. 1. A global damping coefficient of 0.7 was adopted to represent energy dissipation, so that any non-physical oscillation of small-sized particles could be avoided during the DEM simulation.

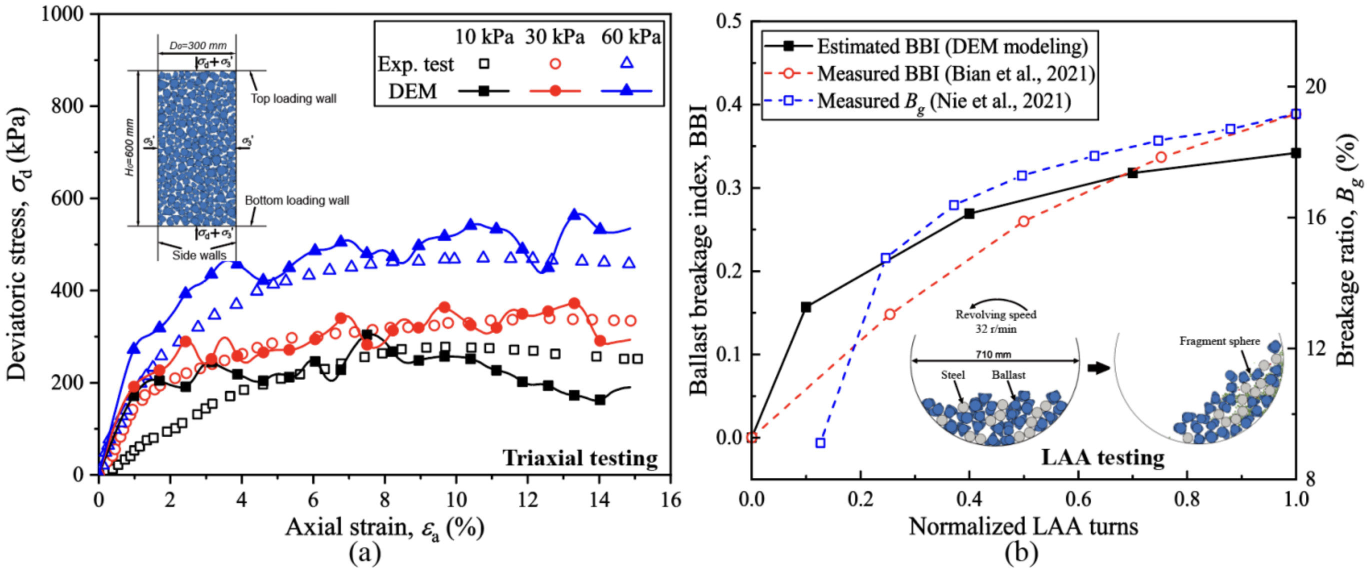


**Fig. 4.** (a) Shear stress-strain responses obtained by DEM modeling and laboratory tests by (Indraratna et al. 2013) in triaxial testing; (b) the estimated BBI compared with the measured BBI by (Bian et al.

2021) and the $B_g$ by (Nie et al. 2021) in LAA testing

Table 1: Micromechanical parameters used in the DEM analysis

| Parameters | Values |
|---|---|
| Ballast density (kg/m$^3$) | 2700 |
| Contact stiffness of ballast, $k_{nb}$, $k_{sb}$ (N/m) | 5.0×10$^8$ |
| Contact stiffness of walls, $k_{nw}$, $k_{sw}$ (N/m) | 1.0×10$^9$ |
| Friction coefficient of ballast, $\mu_b$ | 0.8 |
| Friction coefficient of wall, $\mu_w$ | 0.5 |
| Local damping | 0.7 |

The calibrated parameters were then used in the numerical simulations on the LAA testing. The detailed information about the LAA modeling can refer to (Liu et al. 2021b). Fig. 4(b) shows the estimated Ballast Breakage Index (BBI) with the increase of the normalized LAA turns (defined as the current LAA turns relative to the total LAA turns). As comparison, the BBI by (Bian et al. 2021) and the Marsal's breakage index $B_g$ by (Nie et al. 2021) measured in their laboratory testing are also presented in Fig. 4(b). It is seen that both the DEM modeling and the laboratory testing exhibited comparable trends with an increase in the normalized LAA turns, where the breakage index values (BBI or $B_g$) increased at a diminishing rate, indicating a gradually declining ballast breakage. This is because continuous abrasion causes ballast to become rounder, reducing the breakage possibility of individual ballast particle (Guo et al. 2018; Qian et al. 2017).

Based on the aforementioned calibration and validation, the DEM model used in this study can be justified as being able to accurately represent the mechanical and breakage behaviour of ballast aggregates, and the numerical results generated by the current DEM analysis should have a high credibility for the discussion of particle shape effect.

## 4. Results and Discussions

The direct shearing was then performed on ballast aggregates under four different normal stresses of $\sigma_n$ =15, 35, 55, and 75 kPa until a horizontal displacement of $\Delta_s = 60$ mm was reached. The clump-based particle degradation model was automatically triggered every 200 cycling steps to capture the breakage of ballast particles during shearing. In addition, DEM simulations were also performed without incorporating the degradation model to compare the effects of particle breakage on the macro and microscopic behaviour of ballast aggregates.

*4.1 Shear stress and volumetric deformation*

The predicted shear stress and volumetric deformation for different ballast groups subjected to various normal stresses are presented in Fig. 5 and Fig. 6. The results predicted by the corresponding breakable DEM models are also included to investigate the influence of particle breakage on the shear stress and volumetric deformation. It is seen that the breakable samples exhibit lower shear stresses than their equivalent unbreakable samples, and these differences become greater owing to the elevating particle breakage occurred at higher normal pressures. When ballast breakage is prevented, the aggregate tends to dilate immediately during the shearing; by comparison, significant volumetric compression was observed in all the breakable scenarios, especially in those under higher normal pressures.

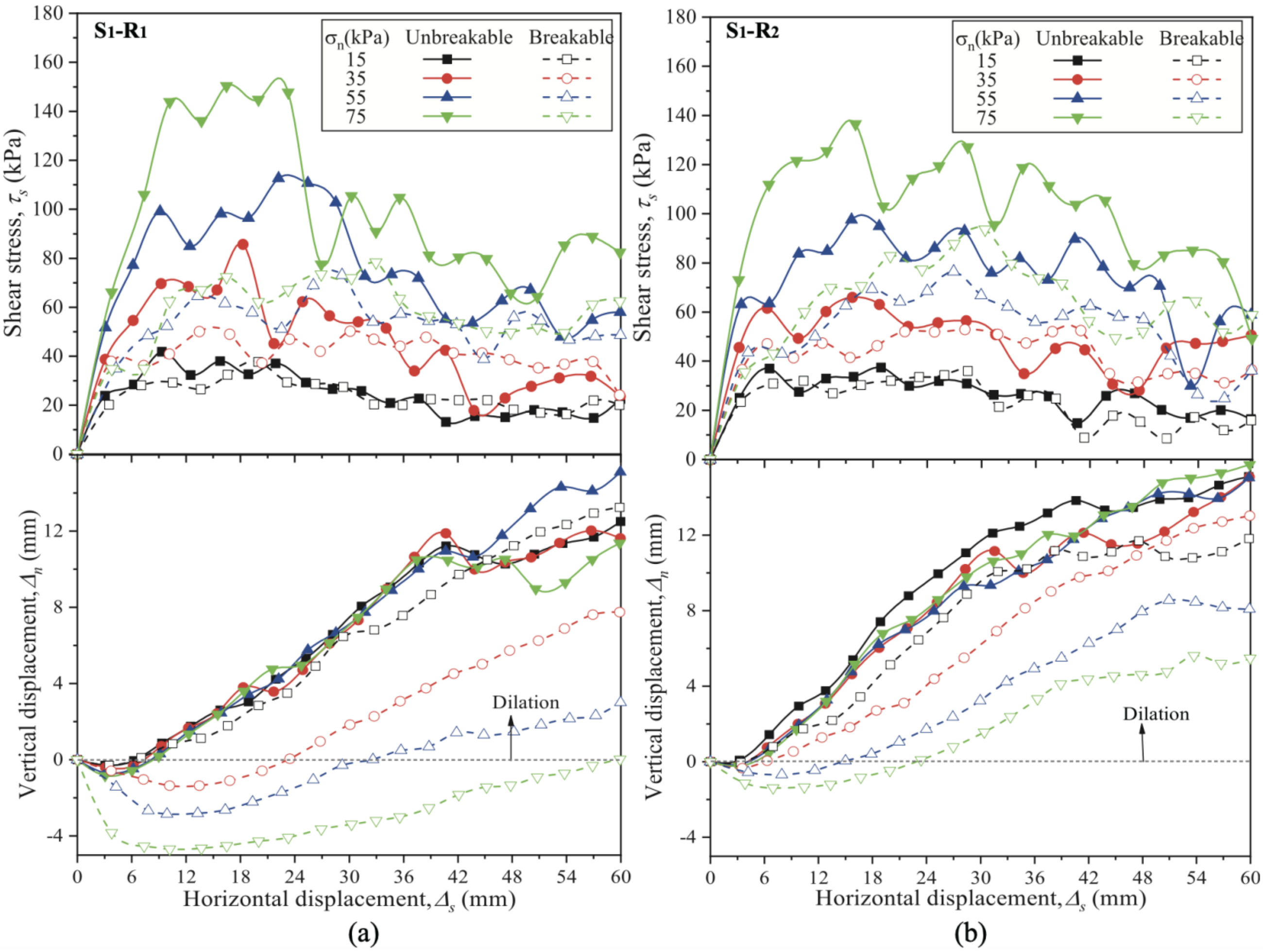


**Fig. 5.** The responses of shear stress and vertical displacement for (a) $S_1 - R_1$; and (b) $S_1 - R_2$

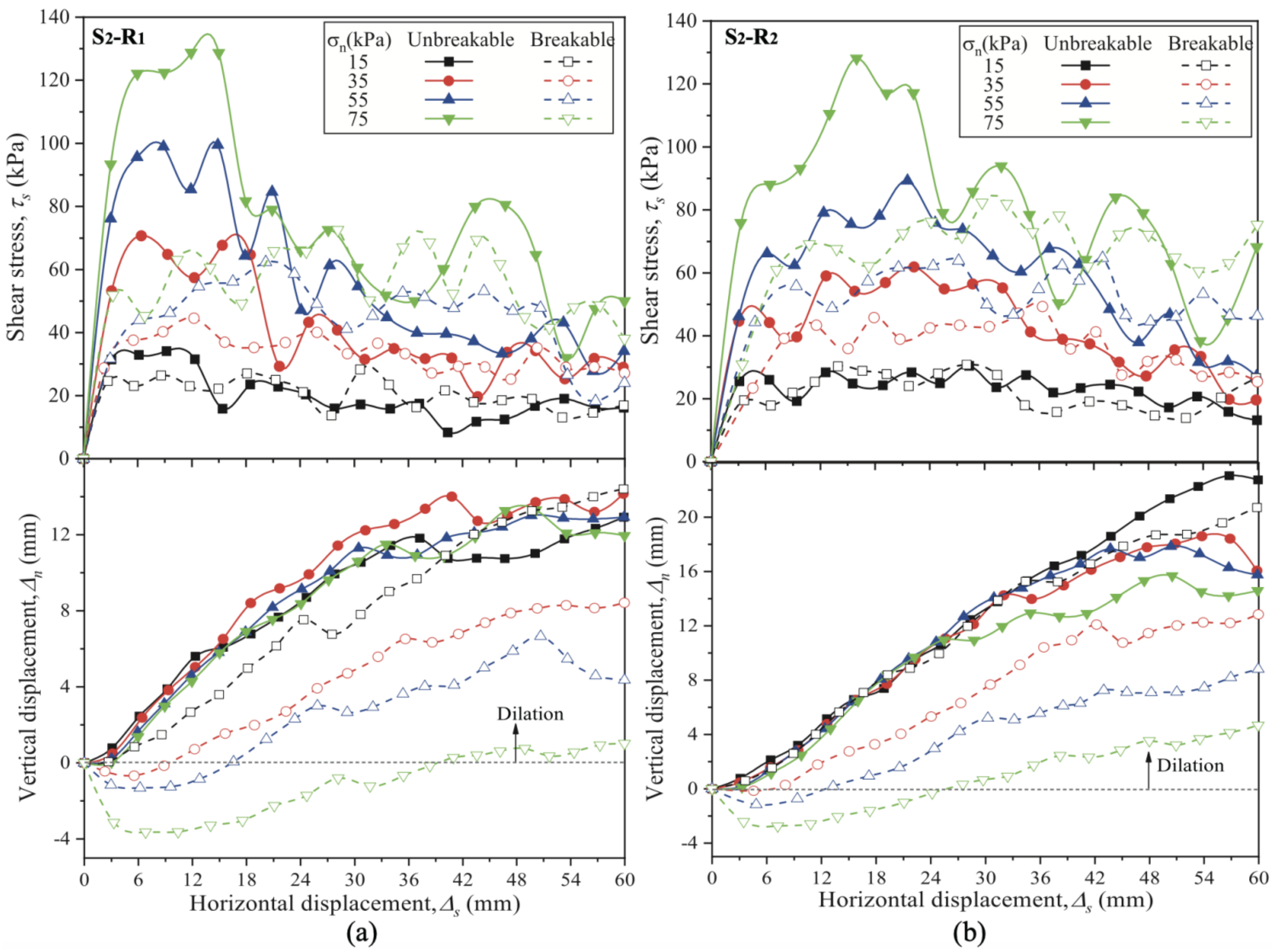


**Fig. 6.** The responses of shear stress and vertical displacement for (a) $S_1 - R_1$; and (b) $S_1 - R_2$

Fig. 7(a1 and a2) shows the strength envelops of ballast aggregates with different particle roundness from low- and high- sphericity groups. Previous studies have shown that the shear strength envelops of granular materials tend to be nonlinear as a result of interparticle interlocking and breakage. In this study, the nonlinear model proposed by (Indraratna et al. 1993) is adopted to examine the shear responses of ballast aggregates, as given:

$$\frac{\tau_p}{\sigma_c} = a(\frac{\sigma_n}{\sigma_c})^b \quad (4)$$

where, the peak shear stress $\tau_p$ and the normal pressure $\sigma_n$ were normalized with the uni-axial compressive strength $\sigma_c = 130$ MPa of parent rock for ballast material; *a* and *b* are two dimensionless parameters. As expected, the strength envelop of ballast aggregate is significantly affected by particle shapes and particle breakage. Considering the unbreakable scenarios, it is seen that the two low-roundness aggregates (i.e., $S_1 - R_1$ and $S_2 - R_1$) obtained higher peak strengths than other groups having similar sphericities but higher roundness (i.e., $S_1 - R_2$ and $S_2 - R_2$). This is because less rounded particles have more angular corners of large curvatures, which can provide resistance during shearing and lead to a higher shear strength. In contrast, the breakable samples exhibit lower shear strength than their comparable unbreakable ones due to reduced shearing resistance associated with the breakage of sharp corners. Furthermore, the strength reduction in low-roundness aggregates is greater, which may be due to the increased corner breakage during shearing.

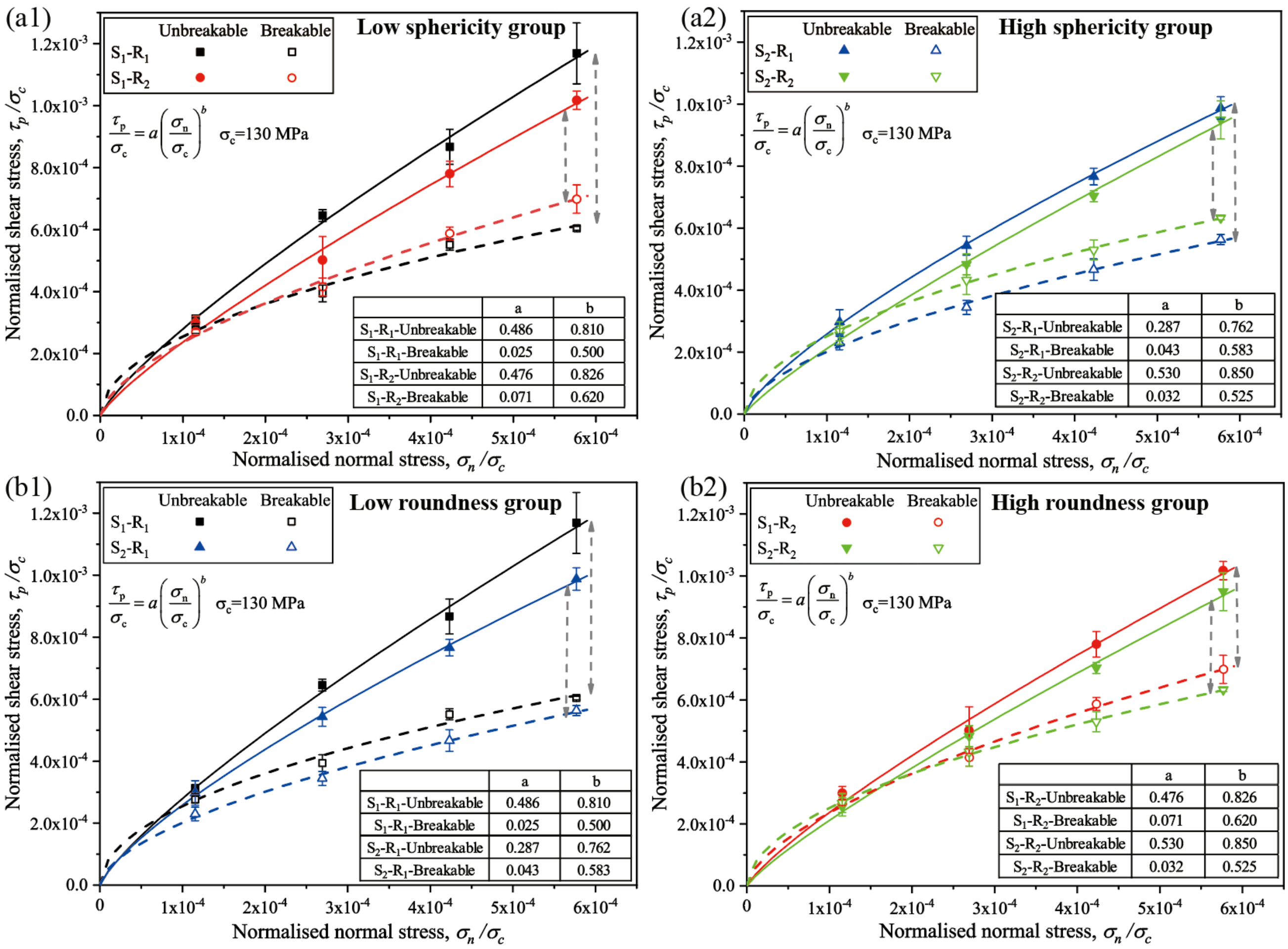


**Fig. 7.** The strength envelops of ballast aggregates from (a1 and a2) low- and high-sphericity group; and (b1 and b2) low- and high-roundness group

Fig. 7(b1 and b2) shows the strength envelops of ballast with various sphericities from low- and high- roundness groups. As expected, the increased irregularity of ballast particles with higher sphericity ($S_1 - R_1$, $S_1 - R_2$) results in higher shear strengths than those with low-sphericity ($S_2 - R_1$, $S_2 - R_2$). Additionally, for two assemblies (either from the low-roundness or high-roundness groups) under a given applied normal stress, the breakage-induced strength decreases are almost identical regardless of their sphericities. This finding implies that the overall particle morphology plays a less significant role in affecting the shear strength development of the ballast aggregate compared to particle corner angularity, which therefore ought to be given greater consideration when selecting ballast materials for railroad construction to ensure better bearing capacity.

### *4.2 Ballast breakage*

Fig. 8 shows the locations of the ballast fragments simulated in DEM (represented by blue dots) for $S_1 - R_2$ at the shearing displacement $\Delta_s$ of 15, 30, 45, 60 mm under $\sigma_n = 75$ kPa. It is shown that the breakage is localised within an inclined zone (width, $d_b$) developing from the rear of the top shearing box to the front of the bottom box, and this zone is observed to become narrower as shearing progresses (i.e., $d_b$=352 and 303 mm at $\Delta_s$=15 and 60 mm, respectively). To quantitatively examine the distribution of ballast fragments, an inclined breakage band within which more than 85% fragments localize is defined. The width $d_b$ and the inclined angle $\beta_b$ of the breakage band for $S_1 - R_2$ at different shearing displacements are presented in Fig. 8. At $\Delta_s = 15$ mm, the $d_b$ is 352 mm, which is about $10.05d_{50}$, with the $\beta_b$ of 16.6° towards the horizontal plane, however, the $d_b$ decreases to 303 mm ($8.66d_{50}$) accompanied by an increase in the $\beta_b$ to 20.6° at $\Delta_s = 60$ mm, indicating a concentrating particle breakage in assemblies during shearing.

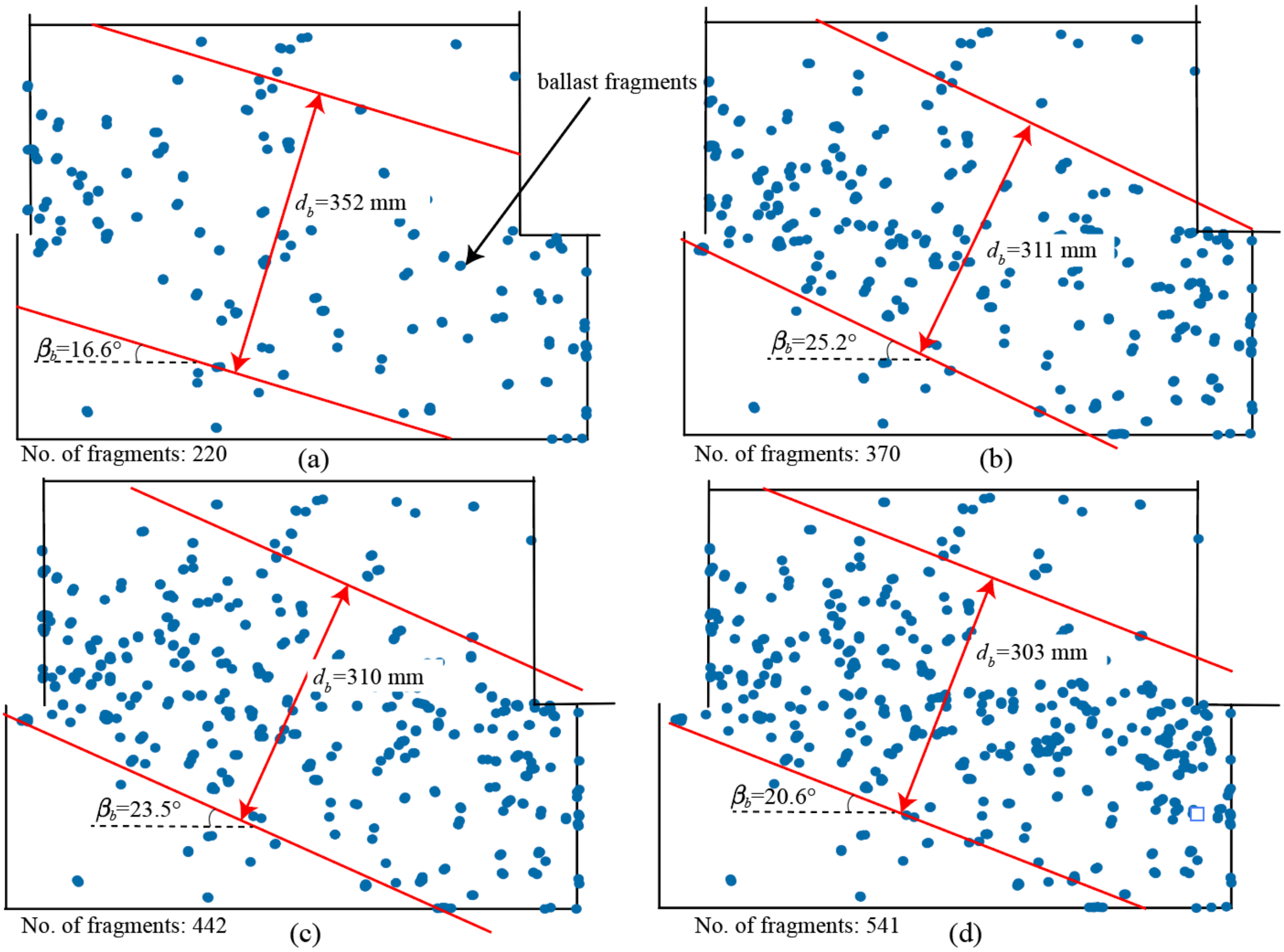


**Fig. 8.** The distribution of ballast fragments in $S_1 - R_2$ under $\sigma_n = 75$ kPa at $\Delta_s$ of (a) 15 mm; (b) 30 mm; (c) 45 mm; and (d) 60 mm

To investigate the influence of particle shape on the amount of breakage, the total volumes of ballast fragments $V_f$ in aggregates having various shapes as shearing develops under $\sigma_n = 75$ kPa are presented in Fig. 9(a). It is seen that the predicted $V_f$ of two low-roundness groups ( $S_1 - R_1$ and $S_2 - R_1$) are greater than that of two high-roundness ones ($S_1 - R_2$ and $S_2 - R_2$), indicating increased particle breakage in less rounded aggregates owing to their increasing corner angularities. In contrast, the breakage in samples with varied sphericity but similar roundness ($S_1 - R_1$ with $S_2 - R_1$, or $S_1 - R_2$ with $S_2 - R_2$) is close during the most shearing phase, except to the $S_2 - R_1$ which obtains a relatively high value of $V_f$ at the end of shearing owing to the continuous breakage of corners with large curvatures.

Fig. 9(b and c) shows the evolution of $d_b$ and $\beta_b$ of ballast aggregates having various particle shapes under $\sigma_n = 75$ kPa. At $\Delta_s$= 6 mm, the $d_b$ of two low-roundness groups ($S_1 - R_1$ and $S_2 - R_1$) are 450 mm (12.86$d_{50}$) and 390 mm (11.14$d_{50}$), respectively, however, that of two high-roundness groups ($S_1 - R_2$ and $S_2 - R_2$) are about 325 mm (9.29$d_{50}$). With the increase of $\Delta_s$, the $d_b$ of $S_1 - R_1$ and $S_2 - R_1$ gradually decrease, and maintain at about 310~325 mm (8.86~9.29$d_{50}$) after the $\Delta_s$ reaches 36 mm. By comparison, the $d_b$ of $S_1 - R_2$ and $S_2 - R_2$ show little variation over the entire shearing process. As for the $\beta_b$, it is seen from Fig. 9(c) that the $\beta_b$ of $S_1 - R_1$ and $S_2 - R_1$ are about 21.6° and 25.3° at $\Delta_s$= 6 mm, respectively; however, the $\beta_b$ of $S_1 - R_2$ and $S_2 - R_2$ are relatively greater, with values of 27.9° and 28.5°. As shearing develops, the $\beta_b$ of $S_1 - R_2$ and $S_2 - R_2$ decrease and maintain at about 18.0° at later stage of shearing. In contrast, the $\beta_b$ of $S_1 - R_1$ and $S_2 - R_1$ experience minor decrease and reach ultimate values of about 23.0°.

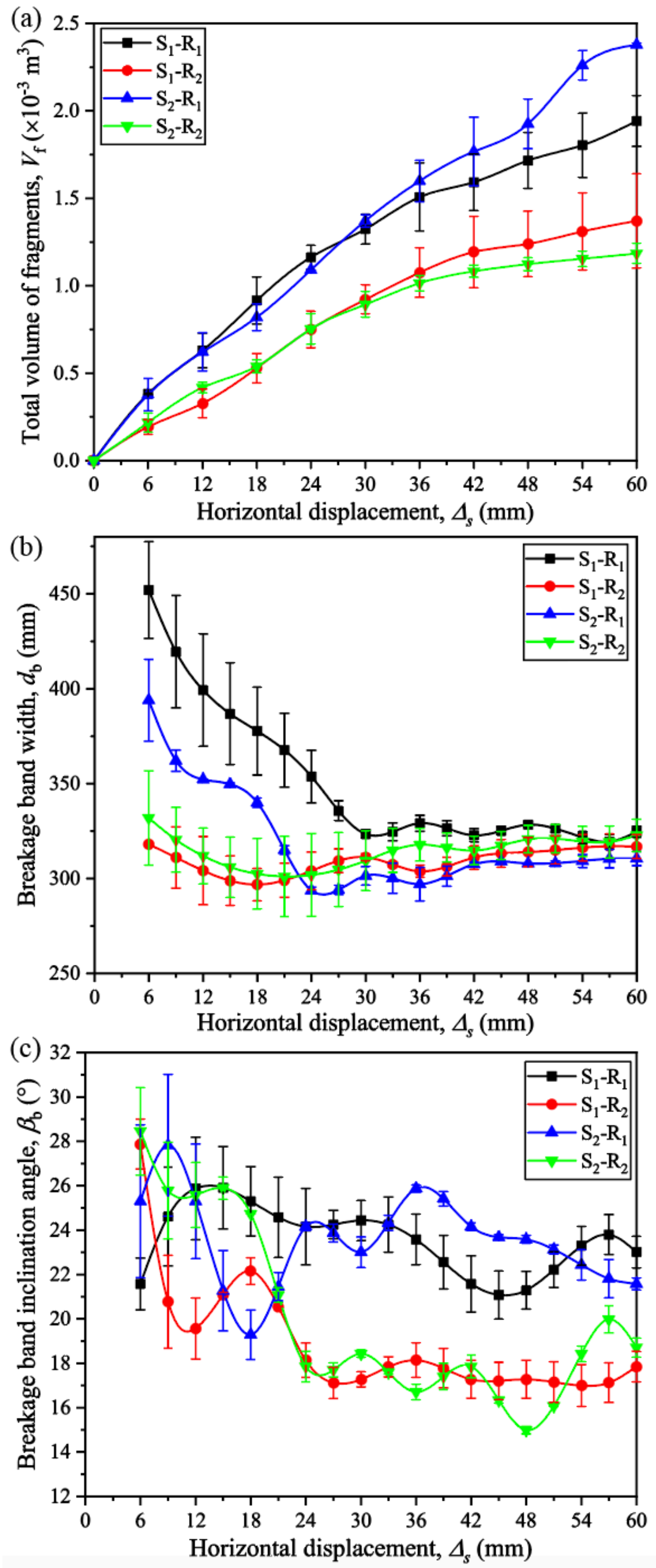


**Fig. 9.** The evolution of (a) total volume of fragments $V_f$; (b) breakage band width $d_b$; and (c) breakage band inclination angle $\beta_b$ of ballast aggregates with various shapes

The breakage band of low-roundness aggregates at the initial stage of shearing is wider than that of high-roundness ones. This is because more particles are broken outside the breakage band (that is the front of the top shearing box and the rear of the bottom shearing box), which results in a more dispersed particle breakage. However, as less rounded particles are more prone to breaking than rounded ones, the subsequent shearing induces an increasing particle breakage within the breakage band region from the rear of the top shearing box to the front of the bottom shearing box in the low-roundness aggregates, causing the breakage band to narrow. In contrast, the overall particle breakage in high-roundness aggregates is comparably lower, and it is observed to be more concentrated near the horizontal plane where large shear deformation occurs, resulting in a smaller inclination angle of the breakage band during shearing. These results imply that particle corner angularity has a greater impact on the breakage of ballast compared to the sphericity, producing more broken fragments distributing across a larger region within the assemblies.

### *4.3 Microscopic responses*

#### *4.3.1 Characteristics of inter-particle interaction*

The distributions of inter-particle contact forces in breakable and unbreakable $S_1 - R_1$ at different shearing displacements ($\Delta_s = 0, 15, 60$ mm) under $\sigma_n = 75$ kPa are shown in Fig. 10. Contacts are represented as solid lines connecting the centroids of two contacting particles, with line thicknesses proportional to contact force magnitudes. The inter-particle contacts within the assembly are homogeneously distributed at the start of shearing ($\Delta_s = 0$ mm). As shearing progresses, the contacts between particles intensify, accompanied by increases in the maximum and the averaged contact force of assemblies, and an obvious band develops from the rear of the top shearing box to the front of the bottom box, within which relatively enhanced inter-particle contacts are localized. In comparison to $\Delta_s = 15$ mm, the inter-particle contacts at the end of shearing (Δs=60 mm) are weaker, with contact forces decreasing, particularly for the unbreakable sample. This microscopic response explains the macroscopic strength softening behaviour after achieving the peak shear stress state, as shown in Fig. 5 and Fig. 6. The breakage of particles also plays a profound effect on the distribution of inter-particle contact, which is stronger and more intensified in the unbreakable sample. This observation implies that when subjected to direct shearing, partilce breakage decreases the intensity of inter-particle contact within the assembly, and therefore reduced shear strengths are expected in breakable samples.

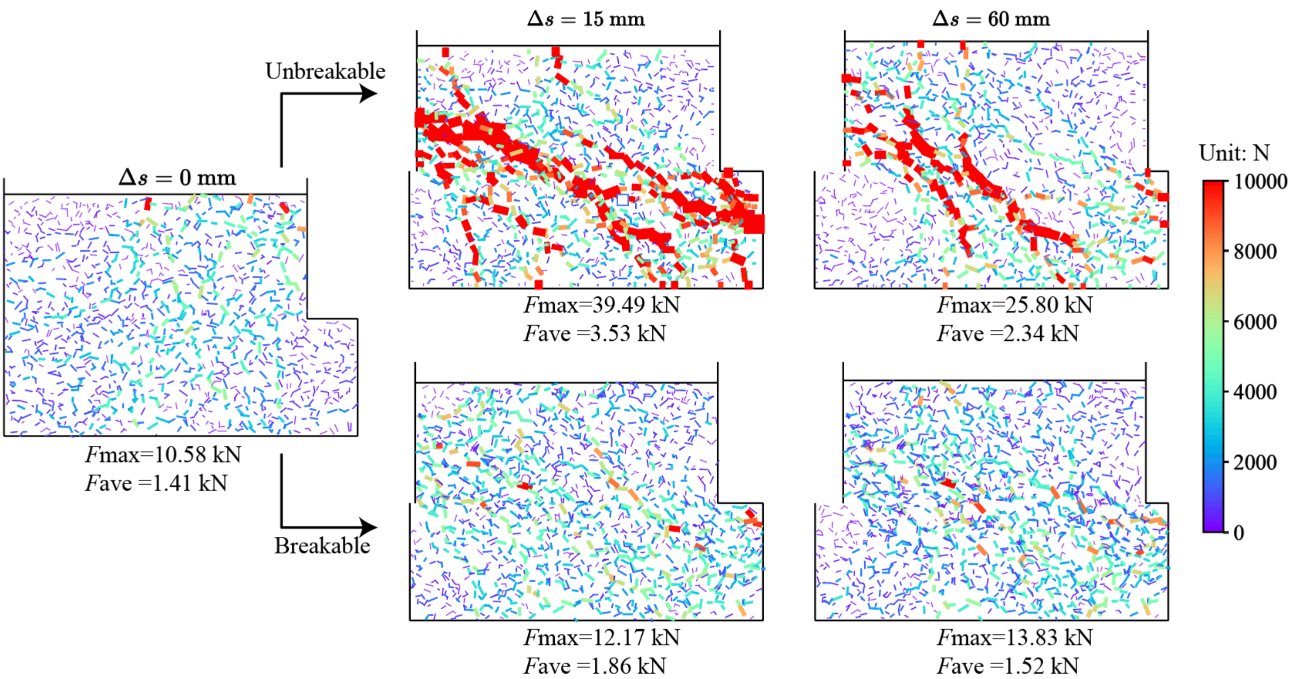


**Fig. 10.** The distributions of inter-particle contact in breakable and unbreakable $S_1 - R_1$ at typical shearing displacements (i.e., $\Delta_s = 0, 15, 60$ mm) under $\sigma_n = 75$ kPa

Fig. 11 shows the distributions of inter-particle contact in unbreakable and breakable samples with different particle shapes at $\Delta_s = 15$ mm and $\sigma_n = 75$ kPa. When breakage is prohibited, it is observed that the distribution of inter-particle contact is significantly affected by particle shape, which is intensified as the sphericity and roundness of the particle inside the assembly decrease. In contrast, when breakage is permitted, the influence of particle shape is diluted, and the distributions of inter-particle contact within the four breakable samples show marginal differences regardless of their sphericity and roundness.

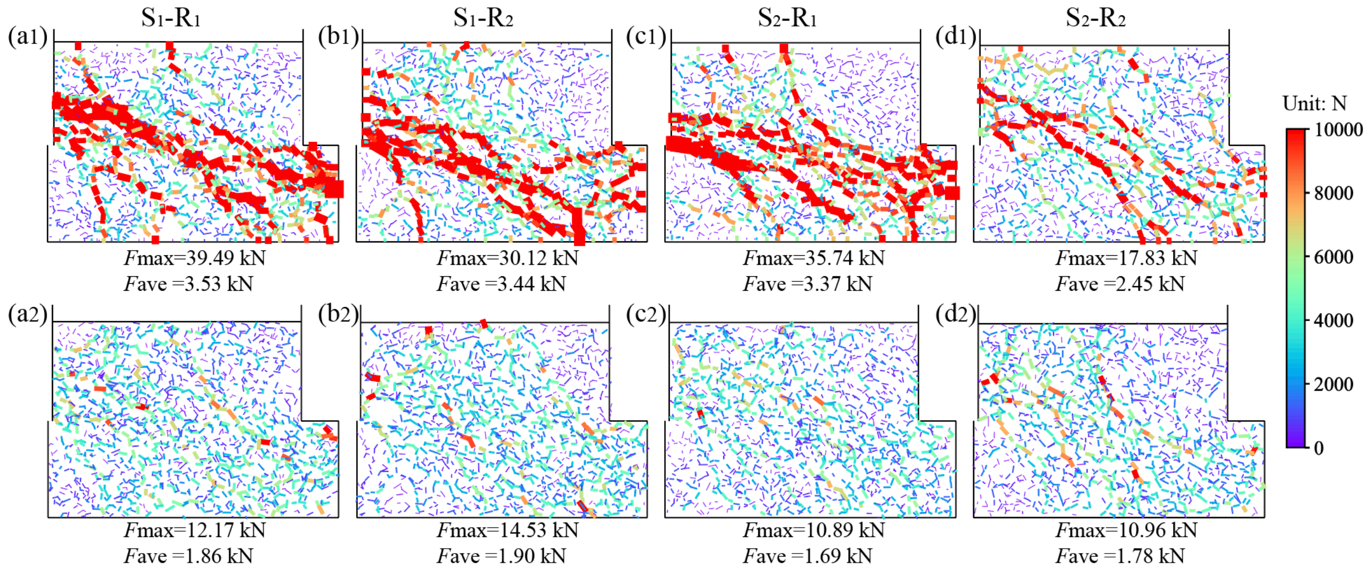


**Fig. 11.** The distributions of inter-particle contact in (a1-d1) unbreakable samples; and (a2-d2) breakable samples at $\Delta_s = 15$ mm under $\sigma_n = 75$ kPa

To investigate the distribution of inter-particle contact force within the assembly, the spatial space is evenly divided into 36 bins of a bin angle of 10°, and the contact force vectors ($f(\omega_i)$) that fall within the *i*-th bin are collected to calculate the distribution density ($P(\omega_i)$) of inter-particle contact force in the *i*-th bin, as given by:

$$P(\omega_i) = \frac{\sum f(\omega_i)}{N_i F_{ave}} \tag{5}$$

where, $N_i$ is the number of inter-particle contacts in the *i*-th bin, $F_{ave}$ is the averaged contact force. The Fourier analysis is performed on the $P(\omega_i)$ based on Rothenburg and Bathurst [5] and Liu et al. [2] to quantify the anisotropy of inter-particle contact forces, as given by:

$$F(\theta_i) = 1 + a\cos 2(\theta_i - \theta_a) + b\cos 4(\theta_i - \theta_a) \tag{5}$$

where, $F(\theta_i)$ is the distribution density of inter-particle contact force at the orientation angle of $\theta_i$; *a*, *b*, and $\theta_a$ are fitting parameters, with the $|a| + |b|$ and $\theta_a$ representing the degree of anisotropy and principal orientation of inter-particle contact force.

Fig. 12 shows the evolution of anisotropy level $|a| + |b|$ and the principal anisotropy orientation

$\theta_a$ for breakable and unbreakable $S_1 - R_1$ under $\sigma_n = 75$ kPa. It is seen that the $|a| + |b|$ and $\theta_a$ of the assemblies rapidly increases to its peak with the onset of shearing. As shearing progresses, the $|a| + |b|$ progressively decreases to a residual value, whilst the $\theta_a$ remains constant until the end of loading. In comparison to unbreakable scenarios, it is seen that the $|a| + |b|$ and $\theta_a$ of breakable scenarios are comparatively lower, indicating that particle breakage reduces the anisotropy of inter-particle contact forces, which is detrimental to the development of shear resistance of the assembly.

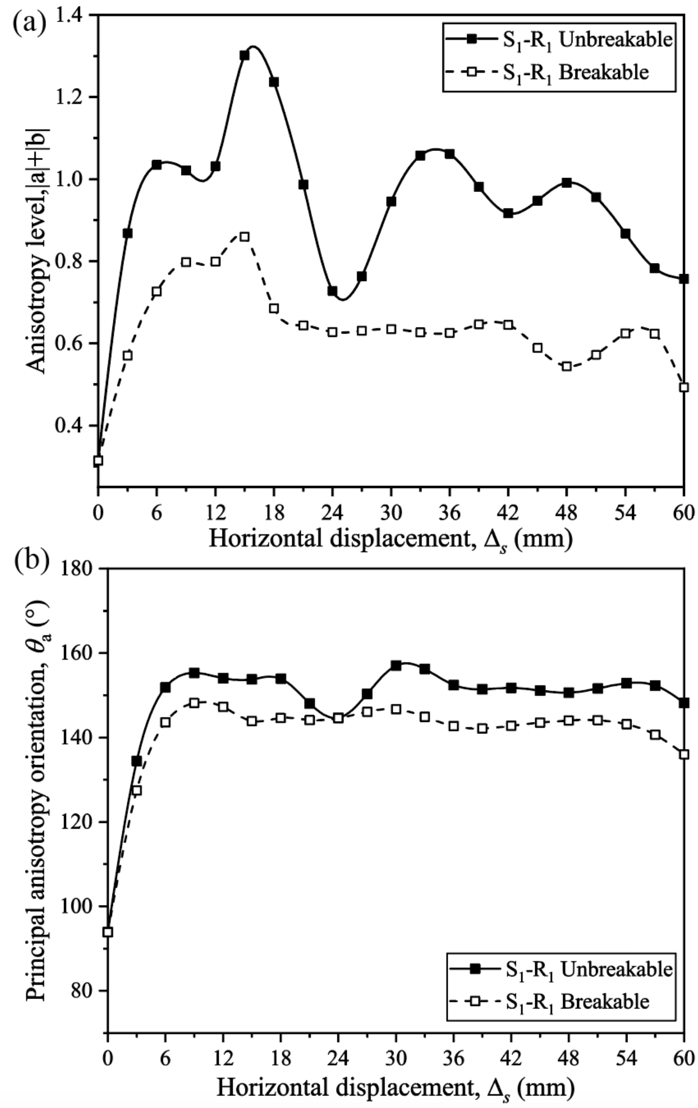


**Fig. 12.** The evolution of (a) anisotropy level $|a| + |b|$; and (b) principal anisotropy orientation $\theta_a$ for unbreakable and breakable $S_1 - R_1$ sample at $\sigma_n = 75$ kPa

Fig. 13 (a1-d1) show the rose diagrams of inter-particle contact forces for the four samples under

$\sigma_n = 75$ kPa before shearing. It is seen that the inter-particle contact forces are vertically distributed in order to support the self-weight of ballast aggregate as well as the applied normal stress. The rose diagrams of inter-particle contact forces for the four samples at $\Delta_s = 15$ mm in unbreakable and breakable scenario are shown in Fig. 13 (a2-d2) and Fig. 13 (a3-d3), respectively. As shearing develops, the inter-particle contact force orientates towards horizontal plane, with an orientation close to that of the contact force distributions as observed in Fig. 11.

The $|a| + |b|$ and $\theta_a$ of each scenario is also presented in Fig. 13. The $|a| + |b|$ of the four samples prior to shearing is relatively small, with a value of around 0.31 ~ 0.47, indicating a low anisotropy level of inter-particle contact forces. The shearing increases the contact force anisotropy as the $|a| + |b|$ increases to 0.85 ~ 1.30 and 0.71 ~ 0.97 for unbreakable and breakable scenario, respectively. Meanwhile, the orientation of principal inter-particle contact force develops from $\theta_a$ of 80.3° ~ 108.2° to 153.8° ~ 165.5° and 141.1° ~ 150.0°. When it comes to the effect of particle shape, it is seen that the differences in $\theta_a$ of assemblies with various particle shapes are marginal. However, a smaller anisotropy level of interparticle contact force is expected within assemblies having higher particle roundness or particle sphericity, which explains the shear strength reduction in assemblies with more spherical and rounder particles as shown in Fig. 7.

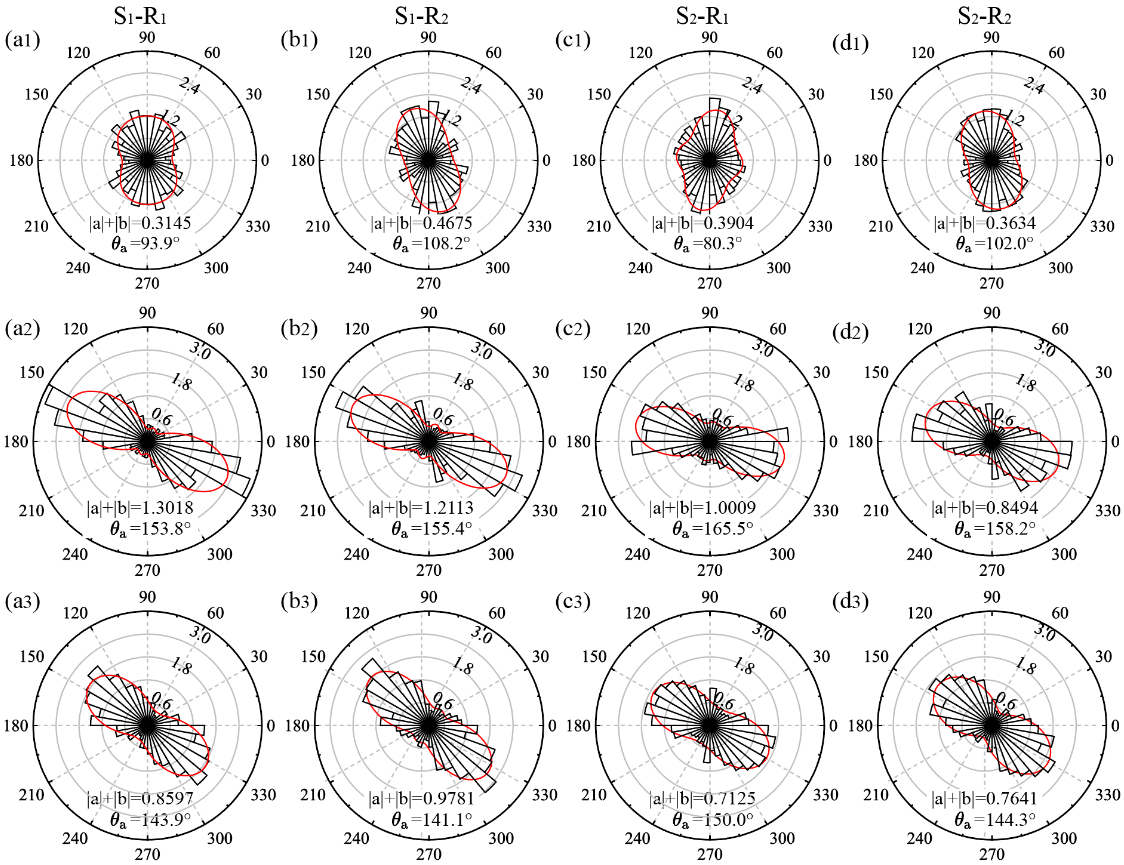


**Fig. 13.** The rose diagrams of inter-particle contact forces for ballast aggregates with various shapes (a1-d1) before shearing; (a2-d2) unbreakable and (a3-d3) breakable samples at $\Delta_s$= 15 mm

According to the analysis of the contact chain distribution and the evolution of anisotropy of contact forces presented above, both the shape and breakage of the particle have a considerable impact on the characteristics of inter-particle interaction performance of ballast assemblies. With the increase of particle sphericity and roundness as well as the permission of particle breakage, the intensity of contact chains and the anisotropy of contact forces of the assembly decrease, consequently resulting in a reduced macroscopic shear strength.

*4.3.2 Characteristics of particle motion*

The characteristics of particle motion in terms of translational displacement and rotation for aggregates with various shapes of are analysed to examine the fundamental mechanism underlying the dilatation of ballast. Fig. 14(a) shows the profiles of particle vertical displacement at $\Delta_s$= $15, 30, 60$ mm for the breakable and unbreakable $S_1 - R_2$ under $\sigma_n = 75$ kPa. Each ballast particle is represented as a dot in the profile, together with information about its position and incremental displacement along the vertical direction (relative to $\Delta_s$= 0 mm). The displacement profiles of the generated ballast fragments after breakage are also included in the figure as represented by gray dots. During the shearing progress, the vertical displacement of ballast aggregate in the bottom box is quite minimal ($<$ 2.5 mm). In comparison, those in the top box and close to the shearing plane exhibit relatively greater vertical incremental displacement, which grows steadily as the shearing progresses. These vertical displacements have been reported as the largest contributor to the volumetric dilation of the ballast assembly.

Fig. 14(b) shows the histogram of the percentage of ballast particles with different vertical displacements for the breakable and unbreakable $S_1 - R_2$ at $\Delta_s$= 60 mm under $\sigma_n = 75$ kPa. It is shown that particle breakage significantly reduces the vertical incremental displacements of ballast aggregates. In the breakable groups, more than 90% of ballast particles exhibit vertical displacements ranging from approximately -2.5 mm to 7.5 mm. Conversely, the unbreakable samples show an increased proportion of particles having greater vertical displacements, ranging from -2.5 mm to 22.5 mm. This phenomenon leads to a restrained volumetric dilation in the breakable samples, as observed in Fig. 5 and Fig. 6. Moreover, a noteworthy observation is that a majority of the ballast fragments undergo negative vertical displacements, especially those near the shear plane. This suggests that the fragments tend to settle down after breaking from their parent ballast particles, further reducing the overall volumetric dilation of the breakable assembly.

Fig. 14(c) shows a box plot comparing the vertical displacements of breakable and unbreakable aggregates with various shapes. The results reveal that aggregates with less spherical shapes ($S_1 - R_1$

and $S_1 - R_2$) or rounder shapes ($S_1 - R_2$ and $S_2 - R_2$) exhibit comparatively greater vertical incremental displacements than highly spherical aggregates ($S_2 - R_1$ and $S_2 - R_2$) or angular aggregates ($S_1 - R_1$ and $S_2 - R_1$). The median vertical displacements for $S_1 - R_1$, $S_1 - R_2$, $S_2 - R_1$, and $S_2 - R_2$ in breakable and unbreakable situations are around 0.38 mm, 1.74 mm, 0.50 mm, 1.96 mm, and 3.46 mm, 5.09 mm, 4.30 mm, 2.35 mm, respectively. This observation suggests that the utilization of ballast aggregates with higher sphericity and lower roundness can help mitigate the volumetric dilation of the assembly.

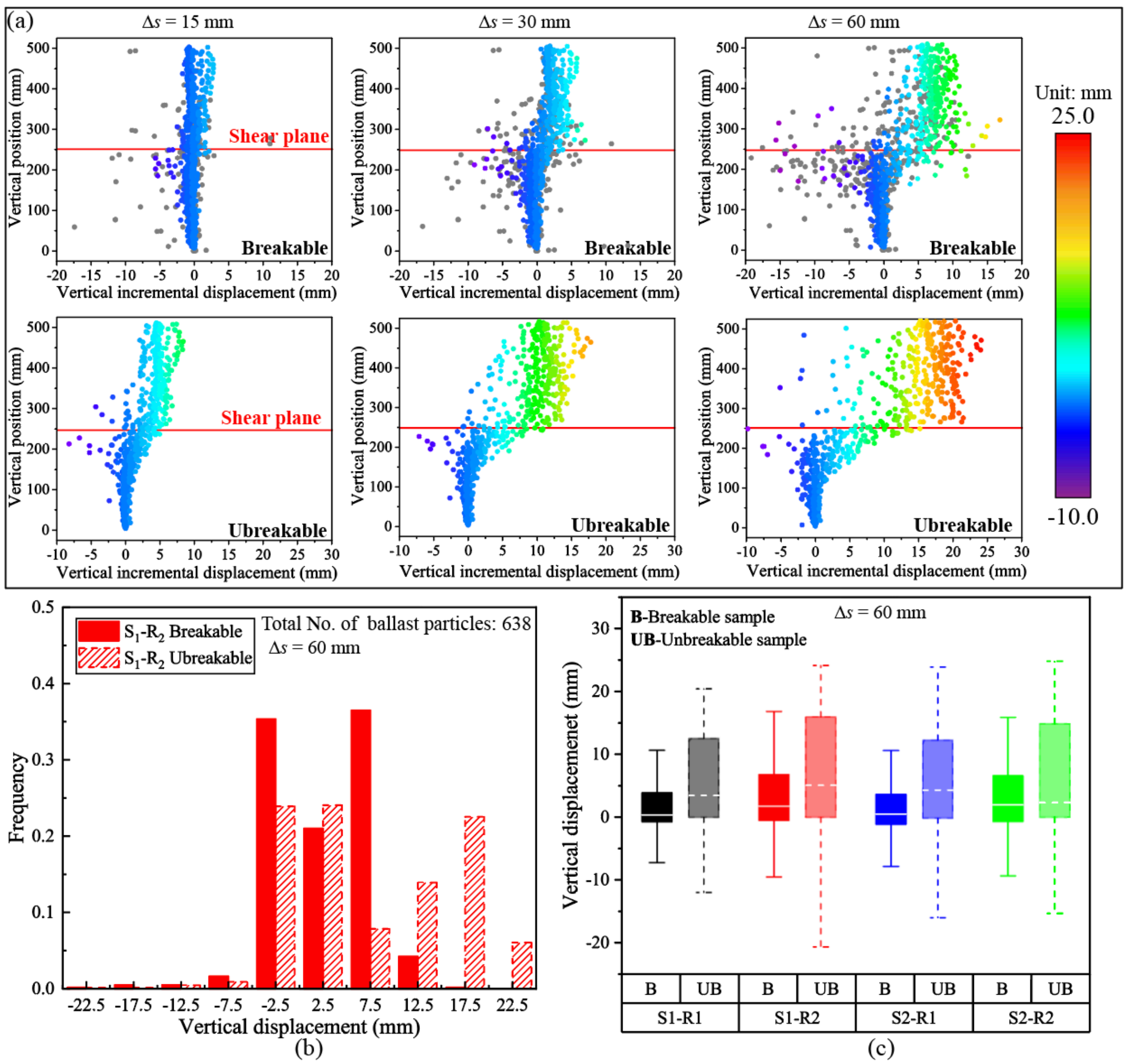


**Fig. 14.** (a) Profiles of particle vertical displacement during the shearing; (b) histogram of the

percentage of ballast particles with different vertical displacements for $S_1 - R_2$; (c) variations of the vertical displacements for different particle groups under $\sigma_n = 75$ kPa

Fig. 15(a) shows the particle incremental rotation angle (relative to $\Delta_s = 0$ mm) for unbreakable and breakable $S_1 - R_2$ at $\Delta_s = 15, 30, 60$ mm when under $\sigma_n = 75$ kPa. Each ballast particle is represented by a circle whose size is proportional to the magnitude of its incremental rotation angle, with transparent and black background colors denoting clockwise and anticlockwise rotation, respectively. With the increase of $\Delta_s$, the incremental rotation angles of the ballast particles steadily rise, and a more profound particle rotation ($> 90°$) is observed within the shear plane area. The incremental rotation of ballast particles is significantly reduced when breakage is allowed. When subjected to shearing forces, particles in an assembly are prone to rolling over their surroundings, however, the climbing and the rotation distance are reduced and compensated because of the breaking of sharp corners and edges that occurs at the local contacting area between two particles, resulting in a smaller particle incremental rotation angle.

Fig. 15(b) shows the histogram depicting the percentage of ballast particles with different incremental rotation angles for the breakable and unbreakable $S_1 - R_2$ aggregates at $\Delta_s = 60$ mm under $\sigma_n = 75$ kPa. It is seen that more than 90% of the ballast particles have incremental rotation angles below 20°. Regarding the effect of particle shape, the box plot in Fig. 15(c) reveals that there is only a slight difference in particle rotation among aggregates with various shapes. The median incremental rotation angles for $S_1 - R_1$, $S_1 - R_2$, $S_2 - R_1$, and $S_2 - R_2$ in breakable and unbreakable groups are 2.34°, 3.27°, 3.42°, 3.46°, and 3.94°, 4.26°, 3.84°, 4.59°, respectively.

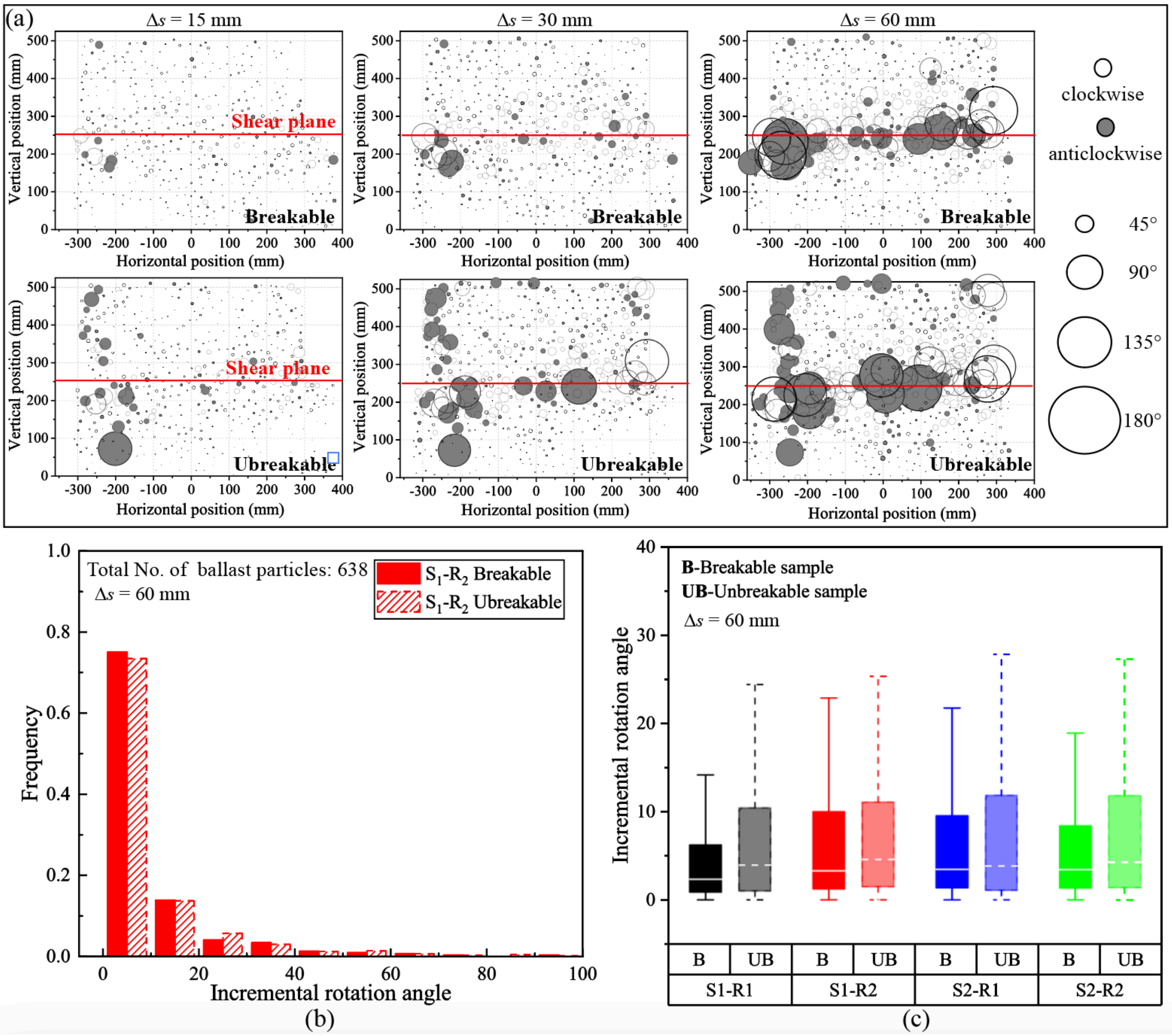


**Fig. 15.** (a) Profiles of particle incremental rotation; (b) histogram of the percentage of ballast particles with different incremental rotation angles for $S_1 - R_2$; (c) variations of the incremental rotation angles for different particle groups under $\sigma_n = 75$ kPa

It can be concluded that both particle shape and breakage influence the characteristics of particle motion during direct shearing, however, the breakage plays a more profound effect on the translational and rotational movement of ballast particles, which are significantly suppressed in all the breaking scenarios, consequently a smaller volumetric dilation is observed for breakable samples compared to their corresponding unbreakable ones.

## 5. Conclusions

This study has examined the shear behaviour of crushable granular materials with various shape sphericities and roundness by using the DEM simulations. The effect of irregular particle shapes on the shear response and the breakage behaviour of a granular assembly was investigated. Detailed microscopic characteristics in terms of anisotropy of internal structures and particle motion were then analysed. The main conclusions which could be drawn from this study are listed below:

1. An improved shear strength was observed in aggregates with lower sphericity and roundness as expected. However, the decrease in particle sphericity (<0.63) and roundness (<0.3) led to an aggravation in particle breakage (hence compromised particle interlocking), which hindered the development of shear strength while reducing the dilation of the granular assembly. This indicates an inevitable trade-off between the shape irregularity and breakage of the particles, and therefore, achieving an optimal balance between the role of shape irregularity and the extent of particle degradation is crucial for enhancing the overall mechanical performance of a granular assembly.

2. When subjected to direct shearing, ballast aggregates experienced continuous grain breakage, which mainly localized within an inclined band in the shear box. As shearing developed, the breakage of particles was gradually concentrated along the shearing plane, causing the width and the inclination angle of this breakage band to decrease to about 310~325 mm (8.86~9.26$d_{50}$) and $18°\sim 23.0°$ towards the shearing plane, respectively. These findings highlight the dynamic nature of particle breakage and its spatial distribution during shearing.

3. The breakage of aggregates is further influenced by the particle shapes especially by the corner roundness. Owing to the extensive abrasion of particle corners with large curvatures, the aggregates with lower roundness show an exacerbated particle breakage, indicated by a wider breakage band (11.14~12.86$d_{50}$) and a greater inclination angle (23.0°) towards the end of shearing. These findings underscore the importance of considering the corner angularity of particles, rather than just their overall morphologies, when selecting ballast material for railroad construction to ensure optimal load-bearing performance. Moreover, the authors believe this to be an important aspect of DEM modelling that cannot be visualized by other means such as through experimental work.

4. At the peak state ($\Delta_s = 15$ mm), the averaged inter-particle contact forces $F_{ave}$ within unbreakable assemblies were about 2.45~3.53 kN, with the corresponding anisotropy level $|a| + |b|$ and the principal anisotropy orientation $\theta_a$ of inter-particle contacts being about 0.85~1.30 and 153.8°~165.5°, respectively. As a result of particle breakage, the $F_{ave}$ decreases to about 1.69~1.90 kN, accompanied by the values of $|a| + |b|$ and $\theta_a$ decreasing to 0.71~0.97 and 141.1°~150.0°, respectively. These results suggest beyond doubt that the compromised shear strength of granular assemblies due to particle breakage is primarily attributed to the weakening and less intensified inter-particle contact network within the aggregates.

5. This study demonstrated that within a granular assembly, both the extent of breakage and shape irregularity influence the displacement of particles. For instance, when there is insignificant breakage, ballast particles experienced an averaged vertical displacement of about 2.35~5.09 mm and an averaged incremental rotation angle of 3.84°~4.59°. These

values decreased to 0.38~1.96 mm and 2.34°~3.46°, respectively, for assemblies showing notable breakage. These results highlight that the suppressed particle motion due to breakage can be the primary cause for reduced volumetric dilation observed in the granular assembly.

For future DEM studies, it is recommended to include more ballast breakage patterns, such as bulk splitting to ensure even a more realistic numerical model for ballast breakage behaviour under various shearing conditions. Furthermore, it is suggested to extend potential future work to more sophisticated 3D modeling, albeit substantially increased computational time and effort. This numerical advancement should offer a more realistic representation of particle shapes irregularities and sizes, and the corresponding particle interactions within the granular assembly, providing a more insightful study of ballast behaviour as a discrete medium.

# Declarations

*Data Availability*

The data used to support the findings of this study are available from the corresponding author upon request.

*Conflicts of Interest*

The authors all declare no conflict of interest.

# Acknowledgments

This work was financially supported by the Chinese Scholarship Council (No. 201906270149) and the continual support of the ARC Industrial Transformation Training Centre, ITTC-Rail through

University of Wollongong and University of Technology Sydney.

## References

Afshar, T., M. M. Disfani, A. Arulrajah, G. A. Narsilio, and S. Emam. 2017. “Impact of particle shape on breakage of recycled construction and demolition aggregates.” *Powder Technology*, 308: 1–12. https://doi.org/10.1016/j.powtec.2016.11.043.

Alshibli, K. A., and M. I. Alsaleh. 2004. “Characterizing Surface Roughness and Shape of Sands Using Digital Microscopy.” *J. Comput. Civ. Eng.*, 18 (1): 36–45. https://doi.org/10.1061/(ASCE)0887-3801(2004)18:1(36).

Altuhafi, F. N., M. R. Coop, and V. N. Georgiannou. 2016. “Effect of Particle Shape on the Mechanical Behavior of Natural Sands.” *Journal of Geotechnical and Geoenvironmental Engineering*, 142 (12): 04016071. American Society of Civil Engineers. https://doi.org/10.1061/(ASCE)GT.1943-5606.0001569.

Bian, X., K. Shi, W. Li, X. Luo, E. Tutumluer, and Y. Chen. 2021. “Quantification of Railway Ballast Degradation by Abrasion Testing and Computer-Aided Morphology Analysis.” *J. Mater. Civ. Eng.*, 33 (1): 04020411. https://doi.org/10.1061/(ASCE)MT.1943-5533.0003519.

Bono, J. P. D., and G. R. McDowell. 2016. “Investigating the effects of particle shape on normal compression and overconsolidation using DEM.” *Granular Matter*, 18 (3): 55. https://doi.org/10.1007/s10035-016-0605-5.

Chen, J., R. Gao, and Y. Liu. 2019. “Numerical Study of Particle Morphology Effect on the Angle of Repose for Coarse Assemblies Using DEM.” *Advances in Materials Science and Engineering*, 2019: 1–15. https://doi.org/10.1155/2019/8095267.

Chen, J., J. S. Vinod, B. Indraratna, N. T. Ngo, R. Gao, and Y. Liu. 2022. “A discrete element study on the deformation and degradation of coal-fouled ballast.” *Acta Geotech.*, 17 (9): 3977–3993. https://doi.org/10.1007/s11440-022-01453-4.

Chen, J., J. S. Vinod, B. Indraratna, T. Ngo, and Y. Liu. 2023. “DEM study on the dynamic responses of a ballasted track under moving loading.” *Computers and Geotechnics*, 153: 105105. https://doi.org/10.1016/j.compgeo.2022.105105.

Cho, G. C., J. Dodds, and J. C. Santamarina. 2006. “Particle shape effects on packing density, stiffness, and strength: Natural and crushed sands.” *J. Geotech. Geoenviron. Eng.*, 132 (5): 591–602. https://doi.org/10.1061/(ASCE)1090-0241(2006)132:5(591).

Coetzee, C. J. 2016. “Calibration of the discrete element method and the effect of particle shape.” *Powder Technology*, 297: 50–70. https://doi.org/10.1016/j.powtec.2016.04.003.

Coop, M. R., K. K. Sorensen, T. B. Freitas, and G. Georgoutsos. 2004. “Particle breakage during shearing of a carbonate sand.” *Géotechnique*, 54 (3): 157–163. https://doi.org/10.1680/geot.2004.54.3.157.

Danesh, A., A. A. Mirghasemi, and M. Palassi. 2020. “Evaluation of particle shape on direct shear mechanical behavior of ballast assembly using discrete element method (DEM).” *Transportation Geotechnics*, 23: 100357. https://doi.org/10.1016/j.trgeo.2020.100357.

Ege, O., and I. Karaca. 2016. “Banach fixed point theorem for digital images.” *J. Nonlinear Sci. Appl.*, 08 (03): 237–245. https://doi.org/10.22436/jnsa.008.03.08.

Gong, J., Z. Nie, Y. Zhu, Z. Liang, and X. Wang. 2019. “Exploring the effects of particle shape and content of fines on the shear behavior of sand-fines mixtures via the DEM." *Computers and Geotechnics*, 106: 161–176. https://doi.org/10.1016/j.compgeo.2018.10.021.

Guo, Y., V. Markine, J. Song, and G. Jing. 2018. "Ballast degradation: Effect of particle size and shape using Los Angeles Abrasion test and image analysis." *Construction and Building Materials*, 169: 414–424. https://doi.org/10.1016/j.conbuildmat.2018.02.170.

Guo, Y., J. Xie, Z. Fan, V. Markine, D. P. Connolly, and G. Jing. 2022. "Railway ballast material selection and evaluation: A review." *Construction and Building Materials*, 344: 128218. https://doi.org/10.1016/j.conbuildmat.2022.128218.

Hamidian, A. H., E. J. Ozumchelouei, F. Feizi, C. Wu, Y. Zhang, and M. Yang. 2021. "A review on the characteristics of microplastics in wastewater treatment plants: A source for toxic chemicals." *Journal of Cleaner Production*, 295: 126480. https://doi.org/10.1016/j.jclepro.2021.126480.

Indraratna, B., N. C. Tennakoon, S. S. Nimbalkar, and C. Rujikiatkamjorn. 2013. "Behaviour of clay-fouled ballast under drained triaxial testing." *Géotechnique*, 63 (5): 410–419. https://doi.org/10.1680/geot.11.P.086.

Indraratna, B., J. S. Vinod, and J. Lackenby. 2009. "Influence of particle breakage on the resilient modulus of railway ballast." *Geotechnique*, 59 (7): 643–646. https://doi.org/10.1680/geot.2008.T.005.

Indraratna, B., L. S. S. Wijewardena, and A. S. Balasubramaniam. 1993. "Large-scale triaxial testing of grey wacke rockfill." *Géotechnique*, 43 (1): 37–51. ICE Publishing. https://doi.org/10.1680/geot.1993.43.1.37.

Jing, G. Q., Y. M. Ji, W. L. Qiang, and R. Zhang. 2020. "Experimental and Numerical Study on Ballast Flakiness and Elongation Index by Direct Shear Test." *Int. J. Geomech.*, 20 (10): 04020169. https://doi.org/10.1061/(ASCE)GM.1943-5622.0001791.

Jo, S.-A., E.-K. Kim, G.-C. Cho, and S.-W. Lee. 2011. "Particle Shape and Crushing Effects on Direct Shear Behavior Using DEM." *Soils and Foundations*, 51 (4): 701–712. https://doi.org/10.3208/sandf.51.701.

Ketterhagen, W. R., M. T. am Ende, and B. C. Hancock. 2009. "Process Modeling in the Pharmaceutical Industry using the Discrete Element Method." *Journal of Pharmaceutical Sciences*, 98 (2): 442–470. https://doi.org/10.1002/jps.21466.

Li, Y. 2013. "Effects of particle shape and size distribution on the shear strength behavior of composite soils." *Bull Eng Geol Environ*, 72 (3): 371–381. https://doi.org/10.1007/s10064-013-0482-7.

Liu, F., M. Ying, G. Yuan, J. Wang, Z. Gao, and J. Ni. 2021a. "Particle shape effects on the cyclic shear behaviour of the soil–geogrid interface." *Geotextiles and Geomembranes*, 49 (4): 991–1003. https://doi.org/10.1016/j.geotexmem.2021.01.008.

Liu, Q.-W., R.-P. Chen, H.-L. Wang, Z.-Y. Yin, and H.-N. Wu. 2022. "Effect of Particle Shape on Soil Arching in the Pile-Supported Embankment by 3D Discrete-Element Method Simulation." *International Journal of Geomechanics*, 22 (4): 04022027. American Society of Civil Engineers. https://doi.org/10.1061/(ASCE)GM.1943-5622.0002313.

Liu, Y., R. Gao, and J. Chen. 2019. "Exploring the influence of sphericity on the mechanical behaviors of ballast particles subjected to direct shear." *Granular Matter*, 21 (4): 94. https://doi.org/10.1007/s10035-019-0943-1.

Liu, Y., R. Gao, and J. Chen. 2021b. "A new DEM model to simulate the abrasion behavior of irregularly-shaped coarse granular aggregates." *Granular Matter*, 23 (3): 61.

https://doi.org/10.1007/s10035-021-01130-5.

Mcdowell, G. R. 2002. “On the Yielding and Plastic Compression of Sand.” *Soils and Foundations*, 42 (1): 139–145. https://doi.org/10.3208/sandf.42.139.

Miao, C. X., J. J. Zheng, R. J. Zhang, and L. Cui. 2017. “DEM modeling of pullout behavior of geogrid reinforced ballast: The effect of particle shape.” *Computers & Geotechnics*, 81: 249–261. https://doi.org/10.1016/j.compgeo.2016.08.028.

Namjoo, A. M., M. Baniasadi, K. Jafari, S. Salam, M. Mohsen Toufigh, and V. Toufigh. 2022. “Studying effects of interface surface roughness, mean particle size, and particle shape on the shear behavior of sand-coated CFRP interface.” *Transportation Geotechnics*, 37: 100841. https://doi.org/10.1016/j.trgeo.2022.100841.

Nie, Z., M. Ashiru, X. Chen, and S. H. Mohamud. 2021. “Appraisal of Railway Ballast Degradation Through Los Angeles Abrasion, Cyclic Loading Tests, and Image Technics.” *Advances in Geotechnical Engineering & Geoenvironmental Engineering*, Sustainable Civil Infrastructures, S. Shu, J. Wang, and M. Souliman, eds., 48–58. Cham: Springer International Publishing.

Nie, Z., C. Fang, J. Gong, and Z.-Y. Yin. 2020. “Exploring the effect of particle shape caused by erosion on the shear behaviour of granular materials via the DEM.” *International Journal of Solids and Structures*, 202: 1–11. https://doi.org/10.1016/j.ijsolstr.2020.05.004.

Nuebel, K., and L. Rothenburg. 1996. “Particle Shape Effect in Stress-Force-Fabric Relationship for Granular Media.” *Journal of the Mechanical Behavior of Materials*, 7 (3): 219–233. De Gruyter. https://doi.org/10.1515/JMBM.1996.7.3.219.

Powers, M. C. 1953. “A New Roundness Scale for Sedimentary Particles.” *SEPM JSR*, Vol. 23. https://doi.org/10.1306/D4269567-2B26-11D7-8648000102C1865D.

Qian, Y., H. Boler, M. Moaveni, E. Tutumluer, Y. M. A. Hashash, and J. Ghaboussi. 2017. “Degradation-Related Changes in Ballast Gradation and Aggregate Particle Morphology.” *J. Geotech. Geoenviron. Eng.*, 143 (8): 04017032. https://doi.org/10.1061/(ASCE)GT.1943-5606.0001706.

Rui, S., Z. Guo, T. Si, and Y. Li. 2020. “Effect of particle shape on the liquefaction resistance of calcareous sands.” *Soil Dynamics and Earthquake Engineering*, 137: 106302. https://doi.org/10.1016/j.soildyn.2020.106302.

Seyyedan, S. M., A. A. Mirghasemi, and S. Mohammadi. 2023. “DEM-XFEM Study of Particle Shape Effect on Particle Breakage of Granular Materials.” *Geotech Geol Eng*, 41 (5): 3115–3137. https://doi.org/10.1007/s10706-023-02448-y.

Sun, Q. D., B. Indraratna, and S. Nimbalkar. 2014. “Effect of cyclic loading frequency on the permanent deformation and degradation of railway ballast.” *Géotechnique*, 64 (9): 746–751. https://doi.org/10.1680/geot.14.T.015.

Sun, Y., and C. Zheng. 2017. “Breakage and shape analysis of ballast aggregates with different size distributions.” *Particuology*, 35: 84–92. https://doi.org/10.1016/j.partic.2017.02.004.

Taghavi, R. 2011. “Automatic clump generation based on mid-surface.” *Continuum and Distinct Element Numerical Modeling in Geomechanics*, 791–7. Melbourne, Australia.

Taiba, A. C., Y. Mahmoudi, M. Belkhatir, and T. Schanz. 2018. “Experimental Investigation into the Influence of Roundness and Sphericity on the Undrained Shear Response of Silty Sand Soils.” *Geotechnical Testing Journal*, 41. https://doi.org/10.1520/GTJ20170118.

Wadell, H. 1933. “Sphericity and Roundness of Rock Particles.” *Journal of Geology*, 41 (3): 310–331.

Wu, K., W. Sun, S. Liu, and G. Cai. 2021. “Influence of particle shape on the shear behavior of superellipsoids by discrete element method in 3D.” *Advanced Powder Technology*, 32 (11): 4017–4029. https://doi.org/10.1016/j.apt.2021.09.001.

Xu, M. Q., N. Guo, and Z. X. Yang. 2021. “Particle shape effects on the shear behaviors of granular assemblies: irregularity and elongation.” *Granular Matter*, 23 (2): 25. https://doi.org/10.1007/s10035-021-01096-4.

Yang, J., and X. D. Luo. 2015. “Exploring the relationship between critical state and particle shape for granular materials.” *Journal of the Mechanics and Physics of Solids*, 84: 196–213. https://doi.org/10.1016/j.jmps.2015.08.001.

Yang, Y., J. F. Wang, and Y. M. Cheng. 2016. “Quantified evaluation of particle shape effects from micro-to-macro scales for non-convex grains.” *Particuology*, 25: 23–35. https://doi.org/10.1016/j.partic.2015.01.008.

Zhang, J., J. Qiao, K. Sun, and Z. Wang. 2022. “Balancing particle properties for practical lithium-ion batteries.” *Particuology*, 61: 18–29. https://doi.org/10.1016/j.partic.2021.05.006.

Zhang, T., C. Zhang, J. Zou, B. Wang, F. Song, and W. Yang. 2020. “DEM exploration of the effect of particle shape on particle breakage in granular assemblies.” *Computers and Geotechnics*, 122: 103542. https://doi.org/10.1016/j.compgeo.2020.103542.

Zhao, S., N. Zhang, X. Zhou, and L. Zhang. 2017. “Particle shape effects on fabric of granular random packing.” *Powder Technology*, 310: 175–186. https://doi.org/10.1016/j.powtec.2016.12.094.

Zheng, J., and R. D. Hryciw. 2015. “Traditional soil particle sphericity, roundness and surface roughness by computational geometry.” *Géotechnique*, 65 (6): 494–506. https://doi.org/10.1680/geot.14.P.192.

Zingg, T. 1935. “Beitrag zur Schotteranalyse.” ETH Zurich.

# List of Figures and Tables

unbreakable and breakable $S_1 - R_1$ sample at $\sigma_n = 75$ kPa

Fig. 13. The rose diagrams of inter-particle contact forces for ballast aggregates with various shapes (a1-d1) before shearing; (a2-d2) unbreakable and (a3-d3) breakable samples at $\Delta_s = 15$ mm

Fig. 14. (a) Profiles of particle vertical displacement during the shearing; (b) histogram of the percentage of ballast particles with different vertical displacements for $S_1 - R_2$; (c) variations of the vertical displacements for different particle groups under $\sigma_n = 75$ kPa

Fig. 15. (a) Profiles of particle incremental rotation; (b) histogram of the percentage of ballast particles with different incremental rotation angles for $S_1 - R_2$; (c) variations of the incremental rotation angles for different particle groups under $\sigma_n = 75$ kPa